Contemporary Mathematics
https://ojs.wiserpub.com/index.php/CM/

UNIVERSAL WISER PUBLISHER

Research Article

Control Strategies for Mittag-Leffler Synchronization in Variable-Order Fractional FitzHugh-Nagumo Reaction-Diffusion Networks

Iqbal H. Jebril[1], Iqbal M. Batiha[1,2], Shaher Momani[2,3], Anjan Biswas[4,5,6,7*]

[1] Department of Mathematics, Al-Zaytoonah University of Jordan, Amman, 11733, Jordan
[2] Nonlinear Dynamics Research Center (NDRC), Ajman University, Ajman, UAE
[3] Department of Mathematics, University of Jordan, Amman, 11942, Jordan
[4] Department of Mathematics & Physics, Grambling State University, Grambling, LA, 71245-2715, USA
[5] Department of Physics and Electronics, Khazar University, Baku, AZ-1096, Azerbaijan
[6] Department of Applied Sciences, Cross-Border Faculty of Humanities, Economics and Engineering, Dunarea de Jos University of Galati, 111 Domneasca Street, Galati, 800201, Romania
[7] Department of Mathematics and Applied Mathematics, Sefako Makgatho Health Sciences University, Medunsa, 0204, Pretoria, South Africa
E-mail: biswas.anjan@gmail.com

Received: 27 June 2025; **Revised:** 21 August 2025; **Accepted:** 4 September 2025

Abstract: This work presents a synchronization control methodology for Variable Fractional-Order Reaction-Diffusion systems (VFO-RDs), focusing on the FitzHugh-Nagumo model. Using Caputo fractional difference operators with time-dependent orders, we design both linear and nonlinear controllers and prove Mittag-Leffler synchronization under explicit constraints. Key contributions: (i) a unified Mittag-Leffler Synchronization (MLSY) framework for variable-order systems using linear and nonlinear controllers; (ii) integration of absolute-state feedback with Lyapunov-based stability for robustness and fast convergence; (iii) demonstration on the FitzHugh-Nagumo (FHN) model, indicating broader applicability in neural engineering.

***Keywords*:** Mittag-Leffler synchronization, variable fractional-order systems, reaction-diffusion systems, Fitzhugh-Nagumo model, nonlinear control, Lyapunov stability

MSC: 65L05, 34K06, 34K28

1. Introduction

Fractional calculus provides a powerful framework for modeling systems with memory and complex dynamics. Recent studies apply it to chaotic systems, epidemiology, and biomedical models [1–5], supported by advanced numerical methods like decomposition and Runge-Kutta Difference Method (RKDM) approaches [6–8]. It also plays a key role in reaction-diffusion systems, control, and hydro-environmental modeling [9–12], reflecting its broad applicability and effectiveness [13].

Discrete Reaction-Diffusion systems (RDs) exhibit complex pattern formation, including localized structures with fronts connecting Turing patterns and Hopf oscillations [14]. These systems display more diverse behaviors than their

DOI: https://doi.org/10.37256/cm.6520257613

continuous counterparts, as perturbations can affect both Turing patterns and Hopf oscillatory domains. The dynamics of discrete RDs are influenced by boundary conditions, which can be studied via asymptotic expansions [15]. In the infinite-medium approximation, fixed points may be classified by their wavelength, and bifurcation diagrams can be constructed for various classes of fixed points and periodic solutions. Although diffusion in spatially continuous systems can lead to blow-up, its effect in discrete systems remains unclear [16]. Nonetheless, Lyapunov-like functions provide sufficient conditions for boundedness in discrete RDs, offering insights into their long-term behavior. Recent research has investigated Fractional-Order (FO) discrete RDs, demonstrating their relevance in fields such as biology. These studies examined the local and global stability of Equilibrium Points (EPs) using linearization and Lyapunov functional approaches. Synchronization dynamics in master-slave configurations have been explored using linear control techniques and fractional discrete Lyapunov methods. Numerical simulations validated theoretical results and demonstrated the impact of discretization and FO on system dynamics [17]. Various numerical schemes, including Fourier spectral methods and exponential time-differencing techniques, have been employed to address stiffness and simulate complex dynamics in multiple dimensions.

The Fractional-Order FitzHugh-Nagumo (FO-FHN) model has been extensively studied in both continuous and discrete settings. Stability properties, dynamics, and numerical solutions have been the focus of many investigations. Armanyos and Radwan [18] compared FO-FHN and Izhikevich neuronal models using nonstandard finite-difference schemes. Brandibur et al. [19] characterized the asymptotic stability of two-dimensional FO difference-equation systems and applied their results to a discrete FHN model. Gafiychuk and Datsko [20] analyzed instabilities and complex dynamics in FO-RDs, showing that FO-FHN-like models can exhibit richer spatiotemporal behavior than standard models. These studies underscore the importance of FO analysis for understanding neuronal dynamics and pattern formation, providing insights into the behavior of discrete and continuous FHN models across various FO orders. Synchronization in FO discrete-time chaotic systems and neural networks has also been explored. Bendoukha et al. [21] demonstrated the coexistence of multiple synchronization types in systems with nonidentical dimensions and orders using nonlinear control schemes. Armanyos et al. [22] investigated synchronization of two coupled neurons via the FHN model in the FO domain, revealing various synchronization patterns. Ouannas et al. [23] proposed two nonlinear control strategies for Θ-Φ synchronization of drive and response systems with differing dimensions. Yang et al. [24] examined synchronization in FO competitive neural networks with RDs terms and time delays, deriving sufficient criteria for global synchronization using a method that combines FO Lyapunov theory and M-matrix techniques. Collectively, these works contribute to understanding synchronization dynamics in FO systems, elucidating control strategies and synchronization phenomena across various neural network models and chaotic systems.

Recent work has concentrated on MLSY in FO systems with RDs terms. Cao et al. [25] studied MLSY for generalized FO-RDs networks via impulsive control, while Stamova and Stamov [26] examined MLSY of FO neural networks with time-varying delays and RDs terms using both impulsive and linear controllers. Narayanan et al. [27] proposed adaptive strategies for MLSY in delayed FO complex-valued RDs neural networks, deriving less conservative algebraic conditions, and also investigated MLSY of FO chaotic systems with unknown parameters and disturbances using adaptive control [28–33]. These studies have developed novel synchronization criteria, often formulated as linear matrix inequalities, and demonstrated their effectiveness through simulations and applications such as image encryption. The main contributions of this research are:

• Design of linear and nonlinear controllers for MLSY in variable FO FitzHugh-Nagumo RDs.
• Lyapunov-based stability analysis establishing MLSY criteria.
• Development of accelerated synchronization strategies with relaxed parameter constraints.
• Numerical validation of spatiotemporal pattern formation and error convergence.
• Comparative analysis of control performance in MLSY synchronization.
• Extension of synchronization frameworks to adaptive FO operators.

The paper is organized as follows: Section 2 introduces mathematical preliminaries on VFO operators. Section 3 describes the master-slave RDs formulation. Section 4 presents the main synchronization theorems and controller designs. Section 5 presents a detailed numerical validation of the proposed synchronization control strategies using finite difference discretization and MATLAB implementation, highlighting both linear and nonlinear control performance across spatiotemporal domains.

2. Preliminaries

We consider the general discrete Variable Fractional-Order (VFO) nonlinear dynamical system given by:

$$\begin{cases} {}^{C}\Delta_{r_0}^{\wp}\Psi(r) \ = \ \lambda\Psi(r+\wp-1)+F\left(r\right), \\ \\ \Psi(r_0)=\Psi_{r_0}, \end{cases} \tag{1}$$

where ${}^{C}\Delta_{r_0}^{\wp}$ denotes the Caputo fractional difference operator with $0<\theta_1\leq\wp\leq\theta_2<1$, $r\in\mathbb{N}_{r_0+\nu-\wp}$, $F:\mathbb{N}_{r_0+\nu-\wp}\times\mathbb{R}^n\to\mathbb{R}^n$ is locally Lipschitz in ϕ, and $\mathbb{R}^n$ is the state space containing the EP $\Psi^*=0$. The EP for system (1) is defined subsequently.

Definition 1 [34] The VFO based on Caputo calculus is defined as:

$$\Delta_{r_0}^{\wp}\varphi(\eta)=\Delta_{r_0}^{-(\nu-\wp)}\Delta^{\nu}\varphi(\eta)=\frac{1}{\Gamma(\nu-\wp)}\sum_{\varsigma=r_0}^{\eta-(\nu-\wp)}(\eta-\varsigma-1)^{\nu-\wp-1}\Delta^{\nu}\varphi(\varsigma), \tag{2}$$

where $\varphi:\mathbb{N}_{r_0}:=\{r_0,\ r_0+1,\ r_0+2,\ \ldots\}\to\mathbb{R}$, $\wp<\mathbb{N}$, $\nu=1+\lceil\wp\rceil$ and $\eta\in\mathbb{N}_{r_0+\nu-\wp}$.

Furthermore, the term $\eta^{(\wp)}$ is given by

$$\eta^{(\wp)}=\frac{\Gamma(\eta+1)}{\Gamma(\eta+1-\wp)}, \quad \wp>0. \tag{3}$$

The associated discrete integral equation can be expressed using the summation:

$$\varphi(\eta)=\varphi_0(\eta)+\frac{1}{\Gamma(\wp)}\sum_{\varsigma=r_0+\nu-\wp}^{\eta-\wp}(\eta-\varsigma-1)^{\wp-1}\varphi(P_\varsigma). \tag{4}$$

where $P_r=r+\wp-1$.

Definition 2 [35] Let $\lambda\in\mathbb{R}$ and let $\theta_2,\ r\in\mathbb{R}$. The discrete MLFs are defined by

$$E_{\theta_2}(\lambda,\ r)\ =\ \sum_{k=0}^{\infty}\frac{\lambda^k\left(r+(k-1)(\theta_2-1)\right)^{(k\theta_2)}}{\Gamma\left(\theta_2 k+1\right)}. \tag{5}$$

Lemma 1 [36] For all $r\in\mathbb{N}_{r_0}$, the following inequality holds:

$${}^{C}\Delta_{r_0}^{\wp}\Psi^2(r)\leq 2\Psi(P_r){}_{r_0}^{C}\Delta_h^{\wp}\Psi(r). \tag{6}$$

Lemma 2 [35] The system (1) admits a unique solution of the form

$$\Psi(r) = \psi_0 E_{\theta_1}(\lambda, r) + \sum_{k=0}^{r-\theta_1} E_{\theta_1}\big(\lambda, r-k-1\big) F(k), \tag{7}$$

where $\wp = \theta_1$.

Definition 3 [37] System (1) is called Mittag-Leffler Stability (MLS) if

$$\big\|\psi(r)\big\| \le \big[m\big(\psi(r_0)\big) E_{\theta_1}(\Lambda, r, r_0)\big]^b, \quad b > 0,\ 0 < \theta_1 < \wp < \theta_2 < 1, \tag{8}$$

The function $m(r)$ is locally Lipschitz continuous in ψ with Lipschitz constant $m_0 > 0$. If the given inequality holds for all initial states $\psi(r_0)$, then system (1) is globally MLS.

Theorem 1 Let $V(r) : [r_0+1, \infty) \times D \to \mathbb{R}$ be locally bounded and locally Lipschitz, where $D \subset \mathbb{R}^n$ is a neighborhood of the origin. Suppose there exist constants $\alpha_1,\ \alpha_2,\ \alpha_3 > 0$ such that, for all $r \in \mathbb{N}_{r_0+1}$ and $0 < \theta_1 < \wp < \theta_2 < 1$,

$$\alpha_1 \big\|\psi\big\|^2 \le V\big(r+\theta_1-1\big) \le \alpha_2 \big\|\psi\big\|^2, \tag{9}$$

$${}^{C}\Delta_{r_0}^{\theta_1} V\big(r\big) \le -\alpha_3 \big\|\psi\big\|^2. \tag{10}$$

Then the EP $\psi^* = 0$ of system (1) is MLS. Moreover, if the inequalities (9)-(10) hold for all $\psi \in \mathbb{R}^n$, then $\psi^* = 0$ is globally MLS.

Proof. Let $\psi(r) = \psi(r, r_0, \psi_0)$ be the solution of system (1). Applying inequalities (9) and (10), we derive:

$${}^{C}\Delta_{r_0}^{\theta_1} V\big(r\big) \le -\omega_3 \|\psi\|^2 \tag{11}$$

$$\le -\frac{\omega_3}{\omega_2} V\big(r+\theta_1-1\big). \tag{12}$$

Introduce a non-negative function $h(r) \ge 0$, such that for all $r \in \mathbb{N}_{r_0+1}$, $r \ge r_0$, it holds:

$${}^{C}\Delta_{r_0}^{\theta_1} V\big(r\big) = -\frac{\omega_3}{\omega_2} V\big(r+\theta_1-1\big) - h(r). \tag{13}$$

Invoking the solution representation from (4), we obtain:

$$V\big(r\big) = V\big(r_0\big) E_{\theta_1}\Big(-\frac{\omega_3}{\omega_2},\ r\Big)$$

$$-\sum_{\varsigma=0}^{r-\theta_2} E_{\theta_1}\Big(-\frac{\omega_3}{\omega_2},\ r-\varsigma-1\Big) h(\varsigma). \tag{14}$$

Since $h(\theta_2 + \varsigma - 1) \geq 0$, the summation term is non-positive, leading to:

$$V(r) \leq V(r_0) E_{\theta_1}\left(-\frac{\omega_3}{\omega_2},\, r\right). \tag{15}$$

Substituting the bounds from (9) into the above inequality, we have:

$$\|\psi\|^2 \leq \frac{1}{\omega_1} V(r), \tag{16}$$

$$V(r_0) \leq \omega_2 \|\psi_0\|^2. \tag{17}$$

Combining these results yields:

$$\begin{aligned} \|\psi\|^2 &\leq \frac{1}{\omega_1} V(r) \\ &\leq \frac{\omega_2}{\omega_1} \|\psi_0\|^2 E_{\theta_1}\left(-\frac{\omega_3}{\omega_2},\, r\right). \end{aligned} \tag{18}$$

Hence

$$\|\psi\| \leq \sqrt{\frac{\omega_2}{\omega_1}} \|\psi_0\| \left[E_{\theta_1}\left(-\frac{\omega_3}{\omega_2},\, r\right)\right]^{1/2}, \tag{19}$$

which satisfies the MLS condition in Definition 3. Therefore, the EP is MLS.

Remarque 1 Beyond the Caputo definition employed in this study, several other fractional derivatives have been proposed to capture various aspects of nonlocal dynamics. The *two-scale fractal derivative* offers a framework rooted in fractal geometry to handle irregular signals with self-similar structures [38]. *He's fractional derivative* is known for its simplicity and ability to represent local fractional operators without requiring singular kernels [39]. Another prominent operator is the *Atangana-Baleanu derivative*, which features a non-singular, non-local Mittag-Leffler kernel, making it advantageous for memory-dependent modeling in anomalous diffusion [40]. These formulations provide rich mathematical tools for generalized modeling. However, in the context of VFO systems with time-dependent dynamics, the Caputo difference operator remains preferable due to its compatibility with initial value formulations and Lyapunov-based stability criteria-especially when modeling the spatiotemporal behavior of the FitzHugh-Nagumo system.

3. System description

The system under investigation comprises coupled Reaction-Diffusion (RD) processes governed by VFO difference operators. The dynamics are initially modeled via a Partial Differential Equation (PDE) with Neumann boundary conditions [27]:

$$
\begin{cases}
\dfrac{\partial^{\wp}\Psi(y,\ r)}{\partial r^{\wp}} = \zeta\Delta\Psi(y,\ r), & y \in \Omega,\ r > 0,\\[2ex]
\dfrac{\partial\Psi}{\partial\eta} = 0, & y \in \partial\Omega,\ r > 0,\\[2ex]
\Psi(y,\ 0) = \Psi_0(y), & y \in \Omega,
\end{cases}
\tag{20}
$$

The fractional-order derivative $\partial^{\theta(r)}/\partial r^{\theta(r)}$ models nonlocal temporal dynamics that cannot be captured by classical integer-order derivatives. In the context of FitzHugh-Nagumo neuronal systems, the order $\theta(r)$ encodes memory effects intrinsic to ion channel kinetics and action potential propagation across neurons. Biological tissues, especially neural ones, exhibit anomalous diffusion where the rate of spatial spread deviates from classical Fickian behavior. The variability in $\theta(r)$ over time reflects temporal heterogeneity and adaptive responses in the neural microenvironment. Thus, the VFO framework allows for modeling the interplay between time-varying memory and diffusion phenomena, offering a more faithful representation of spatiotemporal signal dynamics in neurobiological processes. In the same regard, while Eq. (20) models the temporal memory effects using a variable-order fractional derivative, recent work by Wang and He [41] emphasizes that spatial variables should also be treated fractionally when time is modeled in a non-integer sense. This fractional spatio-temporal consistency arises naturally in fractal systems, where space and time exhibit self-similar properties. Although our present model adopts a classical spatial Laplacian, future extensions could consider incorporating spatial fractional operators-such as the Riesz or Caputo space derivatives-to formulate a more physically consistent and holistic spatio-temporal framework. Such developments may be particularly relevant in modeling neural substrates with fractal geometries or anomalous diffusion profiles.

Recent studies, such as that by He and Liu [42], have shown that fractal dimensions of porous materials significantly affect their mechanical behavior. Analogously, in neuronal tissues, the fractal-like architecture-including dendritic branching and synaptic microstructures-can influence signal propagation and diffusion dynamics. In this context, the variable fractional order $\theta(r)$ can be viewed as a functional proxy for the two-scale fractal dimension of the underlying biological medium. This interpretation enhances the physical relevance of the model, as it accounts for the spatial heterogeneity and memory-induced irregularities inherent in complex neural environments.

Regarding Eq. (20), the spatial domain is discretized in [43] using

$$
y_{i+1} = y_i + h, \quad \text{for} \quad i = 0,\ \ldots,\ m, \tag{21}
$$

The forward difference is given by:

$$
\Delta_h\Psi_i(t) = \frac{\Psi_{i+1}(r) - \Psi_i(r)}{h}, \tag{22}
$$

The second-order spatial derivative is approximated as:

$$
\frac{\partial^2\Psi(y,\ r)}{\partial y^2} \approx \frac{\Psi_{i-1}(r) - 2\Psi_i(r) + \Psi_{i+1}(r)}{h^2}, \tag{23}
$$

or equivalently:

$$\frac{\partial^2 \Psi(y,\ r)}{\partial y^2} \approx \Delta_h^2 \Psi_{i-1}(r). \tag{24}$$

The temporal evolution is then governed by:

$$\frac{\partial^{\wp} \Psi(y,\ r)}{\partial r^{\wp}} = \zeta \Delta_h^2 \Psi_{i-1}(r), \tag{25}$$

with periodic boundary conditions:

$$\Psi_0(r) = \Psi_m(r), \quad \Psi_1(r) = \Psi_{m+1}(r). \tag{26}$$

Remarque 2 It is worth noting that similar fractional reaction-diffusion mechanisms arise in porous media, such as in the fractal-based modeling of recycled aggregate concretes [44]. These systems exhibit complex diffusion behavior due to microstructural heterogeneities, akin to those found in neuronal tissue. In the FHN model, the "porous" and fractal-like architecture of neural substrates affects signal dispersion and local conductivity, thereby justifying the use of fractional operators to capture such spatial and temporal irregularities. This analogy reinforces the generality of our VFO-based approach in modeling diffusion and signal transport across diverse complex media.

The transition from a regular discrete state system to a VFO discrete state system is motivated by the need to:

• **Model complex dynamics:** Variable fractional operators (e.g., Caputo h-difference operators with time-dependent order $\theta(t)$) enable the incorporation of memory effects, hereditary properties, and anomalous diffusion, which are not captured by classical integer-order discrete systems.

• **Enhance synchronization control:** Finite-time or complete synchronization requires adaptive controllers that adjust dynamically over time. The VFO $\theta(t)$ allows the system's evolution to adapt temporally, improving convergence rates and robustness.

• **Address time-varying phenomena:** In systems like RD processes (e.g., glycolysis models or gene regulatory networks), the VFO $\theta(t)$ can represent spatially or temporally varying diffusion rates, nonlinear interactions, or control gains, offering a more flexible framework than fixed-order discretizations.

• **Improve numerical accuracy:** Fractional operators generalize classical difference schemes, enabling precise modeling of systems with non-local or history-dependent dynamics, as seen in the error dynamics (Eq.(32)) and controlled slave systems (Eq. (28)).

This transition is particularly justified for applications requiring adaptive control strategies, memory-dependent behavior, or multi-scale dynamics, as demonstrated in the cited references on VFO discrete synchronization and diffusion processes. The coupled master-slave systems with Caputo VFO difference operators are:

$$\begin{cases} {}^{C}\Delta_{r_0}^{\wp} u_{1,\ i}(r) = \zeta_1 \Delta_h^2 u_{1,\ i-1}(P_r) - u_{1,\ i}^3(P_r) + (\varpi + 1) u_{1,\ i}^2(P_r) - \varpi u_{1,\ i}(P_r) - u_{2,\ i}(P_r), \\ {}^{C}\Delta_{r_0}^{\wp} u_{2,\ i}(r) = \zeta_2 \Delta_h^2 u_{2,\ i-1}(P_r) + \varepsilon u_{1,\ i}(P_r) - \varepsilon \gamma u_{2,\ i}(P_r), \end{cases} \tag{27}$$

and the controlled slave system:

$$\begin{cases} {}^{C}\Delta_{r_0}^{\wp}U_{1,\, i}(r) = \zeta_1 \Delta_h^2 U_{1,\, i-1}(P_r) - U_{1,\, i}^3(P_r) + (\varpi + 1)U_{1,\, i}^2(P_r) - \varpi U_{1,\, i}(P_r) - U_{2,\, i}(P_r) + C_1(r), \\ {}^{C}\Delta_{r_0}^{\wp}U_{2,\, i}(r) = \zeta_2 \Delta_h^2 U_{2,\, i-1}(P_r) + \varepsilon U_{1,\, i}(P_r) - \varepsilon\gamma U_{2,\, i}(P_r). \end{cases} \tag{28}$$

Boundary and initial conditions are given by:

$$U_{k,\, j}(r) = U_{k,\, j+m}(r), \quad k = 1,\ 2,\ j = 0,\ 1. \tag{29}$$

and

$$U_{k,\, i}(0) = g_k(y_i), \quad k = 1,\ 2. \tag{30}$$

The control terms $C_1(r)$ and $C_2(r)$ in the slave system play a pivotal role in steering its dynamics to match those of the master. In particular, these control inputs serve to:

• **Compensate for Nonlinearities and Uncertainties:** The underlying slave dynamics include nonlinear reaction and diffusion terms that, if left unchecked, would cause the slave trajectory to diverge from the master. By introducing carefully designed control signals, one effectively cancels or mitigates these nonlinear effects, ensuring that any discrepancies arising from parameter uncertainties or discretization errors are actively counteracted.

• **Enforce Error Convergence in Finite Time:** Without control, the synchronization error $e_k(r)$ may decay only asymptotically or could even persist due to mismatches in initial conditions. The control system accelerates the error convergence by injecting corrective actions whenever the deviation between master and slave states exceeds a desired threshold. In practice, this means that the slave can "catch up" to the master precisely within a predetermined settling time, which is essential for applications requiring strict timing guarantees.

• **Enhance Robustness and Adaptivity:** Real-world implementation-whether in communication networks, robotic swarms, or chemical reactors-inevitably faces disturbances (e.g., measurement noise, external perturbations, model imperfections). The controllers $C_1(r)$ and $C_2(r)$ are typically constructed to respond dynamically to such disturbances. By continuously adjusting the input based on the instantaneous error, the slave system remains robust against these perturbations, maintaining synchronization even when the environment changes or unforeseen fluctuations occur.

• **Guarantee Practical Applicability of Theoretical Results:** Theoretical proofs of MLS often assume ideal conditions (exact parameters, no external noise). However, when moving from theory to simulation or experimental setup, the control signals ensure that the idealized synchronization criteria translate into real behavior. In other words, the controllers serve as the bridge between "mathematical synchronization" and "observable synchronization," making it feasible to implement the proposed strategies in hardware or software platforms.

• **Provide Flexibility to Meet Design Specifications:** Depending on the specific application-be it rapid synchronization in real-time control systems or energy-efficient synchronization in large-scale networks-the form of $C_1(r)$ and $C_2(r)$ can be tailored to optimize settling time, minimize control effort, or satisfy other performance metrics. This design flexibility allows engineers to balance competing objectives (speed, energy consumption, robustness) and thus adapt the synchronization mechanism to diverse practical scenarios.

Without these control inputs, the slave subsystem would merely evolve according to its intrinsic dynamics, making synchronization with the master either impossible or impractically slow. The controllers are therefore indispensable: they actively drive the error to zero within a finite horizon, counteract uncertainties, and render the theoretical synchronization framework implementable in real-world settings.

The synchronization errors are defined as:

$$e_{k,\,i}(r) = U_{k,\,i}(r) - u_{k,\,i}(r), \quad k = 1,\, 2. \tag{31}$$

with error dynamics:

$$\begin{cases} {}^{C}\Delta_{r_0}^{\wp} e_{1,\,i}(r) = \zeta_1 \Delta_h^2 e_{1,\,i-1}(P_r) - \left[U_{1,\,i}^2 + U_{1,\,i}^2 + U_{1,\,i} U_{1,\,i}\right] e_{1,\,i}(P_r) \\ \qquad\qquad + (\varpi + 1)(U_{1,\,i} + U_{1,\,i}) e_{1,\,i}(P_r) - \varpi e_{1,\,i}(P_r) - e_{2,\,i}(P_r) + C_1(r), \\ {}^{C}\Delta_{r_0}^{\wp} e_{2,\,i}(r) = \zeta_2 \Delta_h^2 e_{2,\,i-1}(P_r) + \varepsilon e_{1,\,i}(P_r) - \varepsilon \gamma e_{2,\,i}(P_r), \end{cases} \tag{32}$$

subject to:

$$e_{k,\,j}(r) = e_{k,\,j+m}(r), \quad k = 1,\, 2, \quad j = 0,\, 1. \tag{33}$$

and initial errors:

$$e_{k,\,i}(0) = \overline{g_k}(y_i) - g_k(y_i), \quad k = 1,\, 2. \tag{34}$$

The control system manages the slave system (32) through a feedback-driven approach that ensures synchronization with the master system. Here's how it operates without mathematical details:

• **Error Monitoring:** Continuously measures the discrepancy between the slave and master system states (e.g., differences in their outputs or variables).

• **Corrective Actions:** Dynamically adjusts the control inputs C_1 and C_2 to counteract mismatches. These inputs actively suppress nonlinearities, uncertainties, and external disturbances in the slave system that could otherwise cause divergence.

• **Finite-Time Convergence:** Ensures synchronization errors vanish within a predetermined time frame by applying aggressive corrective measures when deviations are detected, rather than allowing gradual asymptotic convergence.

• **Adaptability:** Automatically tunes control efforts in response to real-time changes, such as parameter variations or environmental noise, to maintain robustness.

• **Compensation for System Dynamics:** Neutralizes intrinsic slave system behaviors (e.g., nonlinear reactions, diffusion effects) that hinder synchronization, effectively aligning the slave's evolution with the master's trajectory.

By integrating these strategies, the control system bridges theoretical synchronization goals with practical implementation, ensuring reliable and timely coordination between the master and slave systems.

4. Main results

In this section, we present our main synchronization results for the coupled VFO-FHN-RD master-slave system introduced in Section 2. We begin by designing a linear state-feedback controller that guarantees discrete MLS under suitable parameter constraints. We then propose a nonlinear controller that achieves an accelerated synchronization rate and relaxes the parameter restrictions.

Theorem 2 The system (32) achieves MLSY if the linear control is designed as follows:

$$C_1(r) = -\left(3\varsigma^2 + 2(1+\varpi)\varsigma\right) e_{1,\,i}(P_r) + (1-\varepsilon)e_{2,\,i}(P_r). \tag{35}$$

Proof. We construct a Lyapunov function candidate [45]:

$$V(r) = \frac{1}{2}\sum_{i=1}^{m} e_{1,\,i}^2(r) + e_{2,\,i}^2(r), \tag{36}$$

and analyze its fractional difference. Applying Lemma 1 yields:

$$\begin{aligned}
{}^{C}\Delta_{r_0}^{\wp} V(r) &= \frac{1}{2}\sum_{i=1}^{m} {}^{C}\Delta_{r_0}^{\wp}\left(e_{1,\,i}^2 + e_{2,\,i}^2\right) \leq \sum_{i=1}^{m} e_{1,\,i}\,{}^{C}\Delta_{r_0}^{\wp} e_{1,\,i} + e_{2,\,i}\,{}^{C}\Delta_{r_0}^{\wp} e_{2,\,i} \\
&\leq \sum_{i=1}^{m} e_{1,\,i}\Bigg[\zeta_1\Delta_h^2 e_{1,\,i-1} - \left(U_{1,\,i}^2 + U_{1,\,i}^2 + U_{1,\,i}U_{1,\,i}\right)e_{1,\,i} + (\varpi+1)(U_{1,\,i}+U_{1,\,i})e_{1,\,i} \\
&\quad - \varpi e_{1,\,i} - e_{2,\,i} - \left(3\varsigma^2 + 2(1+\varpi)\varsigma\right)e_{1,\,i} + (1-\varepsilon)e_{2,\,i}\Bigg] + \sum_{i=1}^{m} e_{2,\,i}\left[\zeta_2\Delta_{\delta_y}^2 e_{2,\,i-1} + \varepsilon e_{1,\,i} - \varepsilon\gamma e_{2,\,i}(r)\right],
\end{aligned}$$

which gives

$$\begin{aligned}
{}^{C}\Delta_{r_0}^{\wp} V(r) &\leq \sum_{i=1}^{m}\Bigg[\zeta_1 e_{1,\,i}\Delta_{\delta_y}^2 e_{1,\,i-1} - \left(U_{1,\,i}^2 + U_{1,\,i}^2 + U_{1,\,i}U_{1,\,i} + \varpi\right)e_{1,\,i}^2 + (\varpi+1)(U_{1,\,i}+U_{1,\,i})e_{1,\,i}^2 \\
&\quad - \varepsilon e_{1,\,i}e_{2,\,i} - \left(3\varsigma^2 + 2(1+\varpi)\varsigma\right)e_{1,\,i}^2\Bigg] + \sum_{i=1}^{m}\left[\zeta_2 e_{2,\,i}\Delta_h^2 e_{2,\,i-1} + \varepsilon e_{1,\,i}e_{2,\,i} - \varepsilon\gamma e_{2,\,i}^2\right] \\
&\leq \sum_{i=1}^{m} \zeta_1 e_{1,\,i}\Delta_h^2 e_{1,\,i-1} + \zeta_2 e_{2,\,i}\Delta_h^2 e_{2,\,i-1} - \varepsilon\gamma|e_{2,\,i}|^2 + \sum_{i=1}^{m}\Big(|U_{1,\,i}|^2 + |U_{1,\,i}|^2 + |U_{1,\,i}|\,|U_{1,\,i}| - \varpi\Big)|e_{1,\,i}|^2 \\
&\quad + (\varpi+1)\left(|U_{1,\,i}| + |U_{1,\,i}|\right)|e_{1,\,i}|^2 - \sum_{i=1}^{m}\left(3\varsigma^2 + 2(1+\varpi)\varsigma\right)|e_{1,\,i}|^2 \\
&\leq \sum_{i=1}^{m} \zeta_1 e_{1,\,i}\Delta_h^2 e_{1,\,i-1} + \zeta_2 e_{2,\,i}\Delta_h^2 e_{2,\,i-1} - \varepsilon\gamma|e_{2,\,i}|^2 + \left(3\varsigma^2 - \varpi + 2(\varpi+1)\varsigma\right)|e_{1,\,i}|^2 \\
&\quad - \sum_{i=1}^{m}\left(3\varsigma^2 + 2(1+\varpi)\varsigma\right)|e_{1,\,i}|^2 = \sum_{i=1}^{m} \zeta_1 e_{1,\,i}\Delta_h^2 e_{1,\,i-1} + \zeta_2 e_{2,\,i}\Delta_h^2 e_{2,\,i-1} - \varpi|e_{1,\,i}|^2 - \varepsilon\gamma|e_{2,\,i}|^2.
\end{aligned} \tag{37}$$

Applying the summation by parts formula:

$$\sum_{i=a}^{b-1} W_1(i)\,\Delta W_2(i) = W_1(i)\,W_2(i)\,|_a^b - \sum_{y=a}^{b-1} W_2(i+1)\,\Delta W_1(i)\,, \tag{38}$$

Substituting these results back yields:

$$\begin{aligned} {}^{C}\Delta_{r_0}^{\wp} V(r) &\leq -\sum_{i=1}^{m}\left[\zeta_1\,|\Delta_h e_{1,\,i}|^2 + \zeta_2\,|\Delta_h e_{2,\,i}|^2 + \varpi\,|e_{1,\,i}|^2 + \varepsilon\gamma|e_{2,\,i}|^2\right] \\ &\leq -\sum_{i=1}^{m}\left[\zeta_1\,|\Delta_h e_{1,\,i}|^2 + \zeta_2\,|\Delta_h e_{2,\,i}|^2\right] - 2\min\{\varpi,\ \varepsilon\gamma\}\,V(P_r) \leq -2\min\{\varpi,\ \varepsilon\gamma\}\,V(P_r)\,, \end{aligned} \tag{39}$$

Given the operator:

$${}^{C}\Delta_{r_k}^{\theta} V(r) = \frac{1}{\Gamma(1-\theta)} \sum_{s=r_k}^{r-(1-\theta)} (r-s-1)^{\underline{-\theta}} \Delta V(s), \tag{40}$$

we define the weight function $W(\theta)$ derived from the Gamma function ratios:

$$W(\theta) = \frac{1}{\Gamma(1-\theta)} \cdot \frac{\Gamma(r-s-\theta)}{\Gamma(r-s)}. \tag{41}$$

Since $\theta_1 < \theta(t)$, the arguments of the Gamma functions satisfy $r-s-\theta_1 > r-s-\theta(t)$ and $1-\theta_1 > 1-\theta(t)$. Utilizing the monotonicity of the Gamma function for positive arguments, we obtain the inequalities:

$$\Gamma(r-s-\theta_1) > \Gamma(r-s-\theta(t)), \tag{42}$$

$$\Gamma(1-\theta_1) > \Gamma(1-\theta(t)). \tag{43}$$

Given $\Delta V(s) \leq 0$ (indicating $V(r)$ is non-increasing) and the above inequalities, the weights satisfy $W(\theta_2) > W(\theta(t))$. Consequently, for non-positive $\Delta V(s)$, we have:

$$\sum_{s=r_k}^{r+\theta_1-1} W(\theta_2)\Delta V(s) \leq \sum_{s=r_k}^{r+\theta(r)-1} W(\theta(t))\Delta V(s). \tag{44}$$

This implies that the Caputo difference with the smaller order θ_1 dominates the decay rate:

$${}^{C}\Delta_{r_k}^{\theta_1} V(r) \leq {}^{C}\Delta_{r_k}^{\theta(t)} V(r). \tag{45}$$

Therefore, we conclude that:

$$
{}^{C}\Delta_{r_0}^{\theta_1} V(r) \leq -2\min\{\sigma,\ \varepsilon\gamma\} V(P_r)
$$

or

$$
{}^{C}\Delta_{r_0}^{\theta_1} V(r) \leq -2\min\{\sigma,\ \varepsilon\gamma\} V(r+\theta_2-1) \leq -2\min\{\sigma,\ \varepsilon\gamma\}\left(\|e_1(r)\|_2^2+\|e_2(r)\|_2^2\right) = -\min\{\sigma,\ \varepsilon\gamma\}\|e(r)\|_2^2. \quad (46)
$$

Thus, under Theorem 1, the equilibrium point $(e_1,\ e_2)=(0,\ 0)$ is MLS, ensuring synchronization.

The linear state-feedback law (35) guarantees that the synchronization error system (32) converges to the origin with a discrete Mittag-Leffler rate, thereby ensuring robust synchronization between the master and slave processes. Although this linear design is both analytically tractable and computationally efficient, its convergence is asymptotic in the Mittag-Leffler sense. To further enhance performance achieving exact finite-time convergence and relaxing the parameter restrictions-we now develop a nonlinear control scheme in which the error vanishes within a predetermined horizon.

Theorem 3 Consider the error dynamics of the coupled variable fractional-order systems given by (32). If the control inputs $C_1(r),\ C_2(r)$ are designed as as described in [24], then:

$$
\begin{cases}
C_1(r) = -\left(\varsigma^2+(3+2\varpi)\varsigma\right)e_{1,\,i}(P_r)+e_{2,\,i}(P_r)+\varsigma\,\left||U_{1,\,i}(P_r)|-|u_{1,\,i}(P_r)|\right|, \\
C_2(r) = -\varepsilon e_{1,\,i}(P_r)+\dfrac{\varepsilon\gamma}{4}e_{2,\,i}(P_r).
\end{cases} \tag{47}
$$

Then the EP $(e_1,\ e_2)=(0,\ 0)$ of system (32) is achieving MLSY.

Proof. We construct the Lyapunov function candidate (36). Applying Lemma 1 and substituting the error dynamics (32) with the control inputs (47), we obtain:

$$
\begin{aligned}
{}^{C}\Delta_{r_0}^{\wp} V(r) &= \frac{1}{2}\sum_{i=1}^{m} {}^{C}\Delta_{r_0}^{\wp}\left(e_{1,\,i}^2+e_{2,\,i}^2\right) \leq \sum_{i=1}^{m}\left[e_{1,\,i}\,{}^{C}\Delta_{r_0}^{\wp}e_{1,\,i} + e_{2,\,i}\,{}^{C}\Delta_{r_0}^{\wp}e_{2,\,i}\right] \\
&\leq \sum_{i=1}^{m} e_{1,\,i}\Big[\zeta_1\,\Delta_{\delta_y}^2 e_{1,\,i-1} - \left(U_{1,\,i}^2+u_{1,\,i}^2+U_{1,\,i}u_{1,\,i}\right)e_{1,\,i} \\
&\quad + (\varpi+1)\left(u_{1,\,i}+U_{1,\,i}\right)e_{1,\,i} - \varpi e_{1,\,i} - e_{2,\,i} + C_1(r)\Big] \\
&\quad + \sum_{i=1}^{m} e_{2,\,i}\Big(\zeta_2\,\Delta_{\delta_y}^2 e_{2,\,i-1} + \varepsilon e_{1,\,i} - \varepsilon\gamma e_{2,\,i} + C_2(r)\Big) \\
&\leq \sum_{i=1}^{m}\Big[-\left(U_{1,\,i}^2+u_{1,\,i}^2\right)|e_{1,\,i}|^2 - \left(U_{1,\,i}u_{1,\,i}+\varpi\right)|e_{1,\,i}|^2
\end{aligned}
$$

$$
\begin{aligned}
&+ (\varpi+1)\left(u_{1,\,i}+U_{1,\,i}\right)|e_{1,\,i}|^2 - \left(\varsigma^2+(3+2\varpi)\varsigma\right)|e_{1,\,i}|^2 \\
&+ \varsigma\left|U_{1,\,i}-u_{1,i}\right|e_{1,\,i}\Big] - \sum_{i=1}^{m}\frac{3\varepsilon\gamma}{4}|e_{2,\,i}|^2 \\
&\le \sum_{i=1}^{m}\Big[\left(|U_{1,\,i}|\,|u_{1,\,i}|-\varpi+(\varpi+1)\left(u_{1,\,i}+U_{1,\,i}\right)-\left(\varsigma^2+(3+2\varpi)\varsigma\right)\right)|e_{1,\,i}|^2 \\
&+ \varsigma\left|U_{1,\,i}-u_{1,\,i}\right|e_{1,\,i}\Big] - \sum_{i=1}^{m}\frac{3\varepsilon\gamma}{4}|e_{2,\,i}|^2.
\end{aligned}
$$

This, consequently, implies

$$
\begin{aligned}
{}^{C}\Delta_{r_0}^{\wp}V(r) &\le \sum_{i=1}^{m}\Big[\left(\varsigma^2-\varpi+2(\varpi+1)\varsigma-\left(\varsigma^2+(3+2\varpi)\varsigma\right)\right)|e_{1,\,i}|^2 + \varsigma\,|e_{1,\,i}|^2\Big] \\
&- \sum_{i=1}^{m}\frac{3\varepsilon\gamma}{4}|e_{2,\,i}|^2 \\
&\le -2\min\left\{\varpi,\,\frac{\varepsilon\gamma}{4}\right\}V(P_r).
\end{aligned}
\tag{48}
$$

Substituting the control laws and simplifying via the given parameter conditions, we derive:

$$
\begin{aligned}
{}^{C}\Delta_{r_0}^{\theta_1}V(r) &\le -2\min\left\{\varpi,\,\frac{\varepsilon\gamma}{4}\right\}V(r+\theta_1-1) \\
&\le \min\left\{\varpi,\,\frac{\varepsilon\gamma}{4}\right\}\|e(r)\|_2^2.
\end{aligned}
\tag{49}
$$

By Theorem 1, this inequality establishes MLS of the synchronization errors.

5. Numerical simulation

In this section, we implement and evaluate the proposed control strategies using numerical methods. The simulation is carried out using the Finite Difference Method (FDM) to discretize the spatial domain, while the Caputo-type VFO difference operator is used for the temporal evolution. The entire computational framework is developed in Matrix Laboratory (MATLAB) due to its robust support for matrix operations and visualization capabilities. The spatial domain Ω is discretized into m uniform grid points using a mesh step h, and the temporal domain is discretized with a total of N time steps. The second-order central difference scheme is applied to approximate the spatial Laplacian Δ_h^2, and the Caputo fractional difference is evaluated via its discrete convolution representation. Both linear and nonlinear control laws are implemented according to Theorems 2 and 3, respectively. Synchronization is assessed by monitoring the evolution of the synchronization errors $e_{1,\ i}(r)$ and $e_{2,\ i}(r)$, as well as the decay behavior of the discrete Lyapunov function $V(r)$. Parameter values are chosen to satisfy the theoretical stability criteria, and multiple simulation scenarios are conducted to validate robustness under varying fractional orders and nonlinear gains. All figures and tables presented in subsequent subsections are generated using MATLAB's 'surf' and 'plot3' visualization tools, offering a high-resolution depiction of the system's spatiotemporal evolution under different control regimes.

5.1 *Simulation*

This section presents numerical simulations designed to validate the proposed synchronization control strategies for the variable fractional-order FitzHugh-Nagumo reaction-diffusion systems. Two types of controllers are implemented and analyzed: a linear state-feedback controller and a nonlinear control law. The simulations aim to:

5.1.1 *Linear control approach*

The spatial domain and system parameters are configured as:

$$\Omega = [0,\ 30], \quad r \in [0,\ 1], \quad (\zeta_1,\ \zeta_2,\ \varpi,\ \varepsilon,\ \gamma,\ \wp,\ N) = (0.3,\ 0.4,\ 2,\ 0.5,\ 1.75,\ 0.9999\,|\cos(0.05r)|,\ 100). \tag{50}$$

with Initial Conditions (ICs) for the master and slave systems:

$$\begin{cases} g_1(y_i) = 1, \quad g_2(y_i) = 2, \\ \overline{g_1}(y_i) = 1.5, \quad \overline{g_2}(y_i) = 1.5. \end{cases} \tag{51}$$

Figures 1 and 2 display the spatiotemporal pattern formation in the master and slave systems (27)-(28), respectively. The synchronization error dynamics are shown in Figure 3. Using the gain parameter $\varsigma = 0.5$, we implement the linear control law:

$$C_1(r) = -3.75e_{1,\ i}(P_r) + 0.5e_{2,\ i}(P_r), \quad P_r = r + 0.9999\,|\cos(0.05r)| - 1. \tag{52}$$

The parameter constraints in Theorem 1 are satisfied. Figure 4 demonstrates Mittag-Leffler synchronization through the monotonic decay of the Lyapunov function $V(r)$. Furthermore, all tables (Table 1-5) are explicitly cited in the main text to ensure their discussion and relevance are clear.

To further elucidate the spatial and temporal synchronization dynamics, we now provide an expanded tabular presentation of the pattern evolution and control behavior. The following sequence of tables captures detailed spatiotemporal data of the system's trajectories and synchronization responses across different slices and perspectives. These tabulated results reinforce the effectiveness of the proposed linear control strategy in mitigating spatial dispersion and enforcing synchronization.

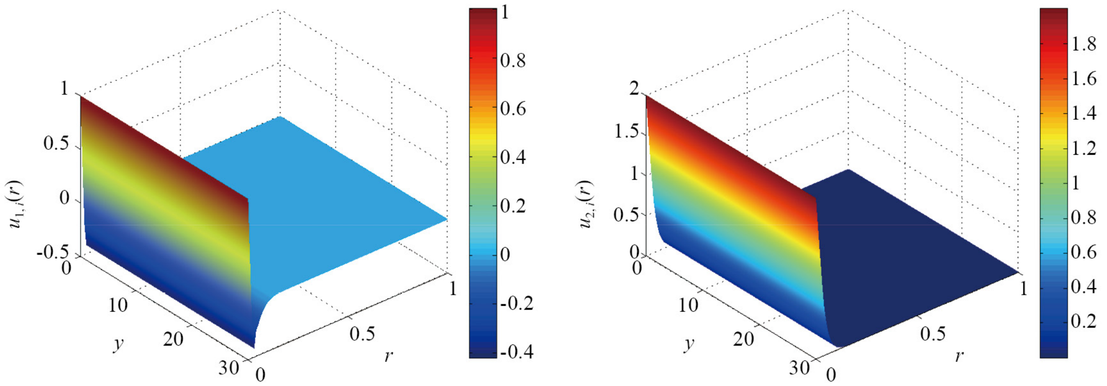

Figure 1. Spatiotemporal trajectories of the master system variables $u_{1,\,i}(r)$ and $u_{2,\,i}(r)$. The plots illustrate how the uncontrolled FitzHugh-Nagumo dynamics evolve over time r and spatial index y in the absence of synchronization control. Note that both components exhibit temporal decay and spatial dispersion typical of reaction-diffusion processes

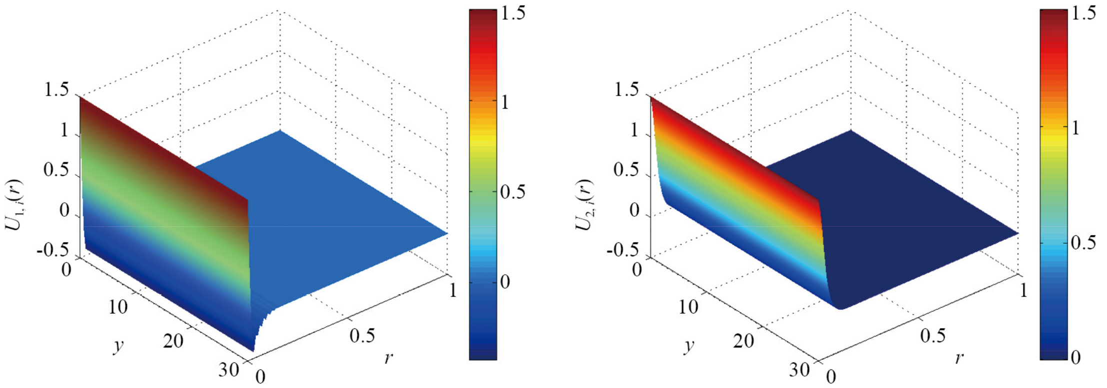

Figure 2. Spatiotemporal trajectories of the slave system variables $U_{1,\,i}(r)$ and $U_{2,\,i}(r)$ under linear control. These plots confirm that the slave dynamics closely follow the master system over time r and spatial index y, indicating successful synchronization via linear state feedback

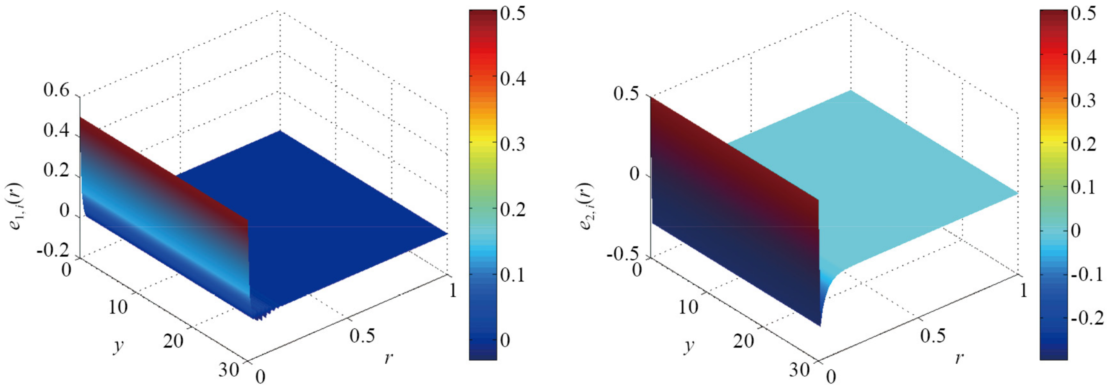

Figure 3. Spatiotemporal trajectories of the synchronization errors $e_{1,\,i}(r) = U_{1,\,i}(r) - u_{1,\,i}(r)$ and $e_{2,\,i}(r) = U_{2,\,i}(r) - u_{2,\,i}(r)$ under linear control. The errors decay toward zero over time r and spatial index y, confirming the achievement of Mittag-Leffler synchronization

Table 1. Detailed spatiotemporal data of master and slave variables for different time slices under linear control

r	$u_{1,\,i}(r)$	$u_{2,\,i}(r)$	$U_{1,\,i}(r)$	$U_{2,\,i}(r)$	$e_{1,\,i}(r)$	$e_{2,\,i}(r)$
0	1	1	1.5000	1.5000	0.5000	0.5000
0.0101	0.4000	1.6250	0.5249	1.3312	0.1250	-0.2937
0.0202	-0.2027	1.2584	-0.1694	1.0605	0.0333	-0.1979
0.0303	-0.4191	0.8977	-0.4257	0.7567	-0.0066	-0.1410
0.0404	-0.2567	0.5392	-0.2246	0.4943	-0.0321	-0.1050
0.0505	-0.2180	0.4035	-0.2411	0.3308	-0.0231	-0.0726
0.0606	-0.1623	0.2649	-0.1240	0.2079	0.0383	-0.0570
0.0707	-0.1194	0.1711	-0.1492	0.1347	-0.0298	-0.0363
0.0808	-0.0857	0.1083	-0.0510	0.0770	0.0347	-0.0313
0.0909	-0.0600	0.0670	-0.0849	0.0492	-0.0249	-0.0179
0.1010	-0.0408	0.0405	-0.0167	0.0236	0.0241	-0.0169
0.1111	-0.0269	0.0238	-0.0432	0.0149	-0.0162	-0.0089
0.1212	-0.0172	0.0135	-0.0031	0.0045	0.0141	-0.0090
0.1313	-0.0107	0.0074	-0.0198	0.0029	-0.0092	-0.0045
0.1414	-0.0064	0.0039	0.0012	-8.1186e-04	0.0076	-0.0047
0.1515	-0.0037	0.0019	-0.0005	-4.0128e-04	-0.0048	-0.0023
0.1616	-0.0020	8.9761e-04	0.0019	-0.0016	0.0039	-0.0025
0.1717	-0.0011	3.7808e-04	-0.0035	-8.4914e-04	-0.0025	-0.0012
0.1818	-3.5448e-04	1.3808e-04	0.0014	-0.0011	-0.0020	-0.0013
0.1919	-2.4831e-04	4.0918e-05	-0.0015	-6.0950e-04	-0.0012	-6.5042e-04
0.2020	-1.0490e-04	1.1552e-05	8.9865e-04	-6.5882e-04	0.0010	-6.7038e-04
0.2121	-3.8767e-05	1.0885e-05	-6.6145e-04	-3.3735e-04	-6.2269e-04	-3.4824e-04
0.2222	-1.2121e-05	1.9885e-05	4.9602e-04	-3.3467e-04	5.0814e-04	-3.5455e-04
0.2323	-4.1577e-06	3.0168e-05	-3.1551e-04	-1.5930e-04	-3.1135e-04	-1.8947e-04
0.2424	-4.0495e-06	3.8661e-05	2.5408e-04	-1.5194e-04	2.5813e-04	-1.9061e-04
0.2525	-6.5421e-06	4.4710e-05	-1.6138e-04	-6.1238e-05	-1.5484e-04	-1.0595e-04
0.2626	-9.3374e-06	4.8612e-05	1.2262e-04	-5.6818e-05	1.3196e-04	-1.0543e-04
0.2727	-1.1605e-05	5.0926e-05	-8.7784e-05	-1.1059e-05	-7.6178e-05	-6.1985e-05
0.2828	-1.3181e-05	5.2182e-05	5.5089e-05	-8.9654e-06	6.8270e-05	-6.1147e-05
0.2929	-1.4157e-05	5.2791e-05	-5.0804e-05	1.3953e-05	-3.6647e-05	-3.8838e-05
0.3030	-1.4695e-05	5.3040e-05	2.1421e-05	1.4925e-05	3.6116e-05	-3.8115e-05
0.3131	-1.4946e-05	5.3112e-05	-3.1719e-05	2.6454e-05	-1.6774e-05	-2.6659e-05
0.3232	-1.5023e-05	5.3118e-05	4.8636e-06	2.6974e-05	1.9887e-05	-2.6144e-05
0.3333	-1.5008e-05	5.3119e-05	-2.1782e-05	3.2851e-05	-6.7741e-06	-2.0268e-05
0.3434	-1.4950e-05	5.3147e-05	-3.2465e-06	3.3205e-05	1.1703e-05	-1.9942e-05
0.3535	-1.4879e-05	5.3217e-05	-1.6611e-05	3.6277e-05	-1.7325e-06	-1.6940e-05
0.3636	-1.4812e-05	5.3332e-05	-7.2252e-06	3.6575e-05	7.5869e-06	-1.6757e-05
0.3737	-1.4757e-05	5.3494e-05	-1.3936e-05	3.8252e-05	8.2172e-07	-1.5241e-05
0.3838	-1.4718e-05	5.3698e-05	-9.1891e-06	3.8539e-05	5.5292e-06	-1.5159e-05
0.3939	-1.4695e-05	5.3942e-05	-1.2566e-05	3.9527e-05	2.1293e-06	-1.4415e-05
0.4040	-1.4688e-05	5.4222e-05	-1.0173e-05	3.9820e-05	4.5148e-06	-1.4402e-05
0.4141	-1.4696e-05	5.4535e-05	-1.1882e-05	4.0474e-05	2.8136e-06	-1.4061e-05
0.4242	-1.4716e-05	5.4878e-05	-1.0686e-05	4.0784e-05	4.0304e-06	-1.4095e-05
0.4343	-1.4749e-05	5.5249e-05	-1.1562e-05	4.1281e-05	3.1872e-06	-1.3968e-05

Table 2. Further spatial refinement showing synchronized trajectories from additional viewpoints, confirming coherence across the domain

r	$u_{1,\,i}(r)$	$u_{2,\,i}(r)$	$U_{1,\,i}(r)$	$U_{2,\,i}(r)$	$e_{1,\,i}(r)$	$e_{2,\,i}(r)$
0.4444	-1.4793e-05	5.5645e-05	-1.0977e-05	4.1612e-05	3.8163e-06	-1.4033e-05
0.4545	-1.4847e-05	5.6064e-05	-1.1440e-05	4.2043e-05	3.4071e-06	-1.4021e-05
0.4646	-1.4910e-05	5.6505e-05	-1.1169e-05	4.2395e-05	3.7410e-06	-1.4110e-05
0.4747	-1.4982e-05	5.6965e-05	-1.1430e-05	4.2803e-05	3.5517e-06	-1.4162e-05
0.4848	-1.5061e-05	5.7444e-05	-1.1323e-05	4.3178e-05	3.7377e-06	-1.4267e-05
0.4949	-1.5147e-05	5.7941e-05	-1.1486e-05	4.3585e-05	3.6603e-06	-1.4356e-05
0.5051	-1.5239e-05	5.8453e-05	-1.1467e-05	4.3980e-05	3.7726e-06	-1.4473e-05
0.5152	-1.5338e-05	5.8980e-05	-1.1586e-05	4.4396e-05	3.7523e-06	-1.4584e-05
0.5253	-1.5442e-05	5.9522e-05	-1.1614e-05	4.4810e-05	3.8282e-06	-1.4712e-05
0.5354	-1.5551e-05	6.0076e-05	-1.1714e-05	4.5238e-05	3.8374e-06	-1.4838e-05
0.5455	-1.5666e-05	6.0643e-05	-1.1770e-05	4.5670e-05	3.8955e-06	-1.4973e-05
0.5556	-1.5784e-05	6.1222e-05	-1.1864e-05	4.6112e-05	3.9203e-06	-1.5109e-05
0.5657	-1.5907e-05	6.1811e-05	-1.1937e-05	4.6560e-05	3.9700e-06	-1.5252e-05
0.5758	-1.6034e-05	6.2411e-05	-1.2031e-05	4.7016e-05	4.0031e-06	-1.5395e-05
0.5859	-1.6165e-05	6.3021e-05	-1.2116e-05	4.7478e-05	4.0491e-06	-1.5543e-05
0.5960	-1.6299e-05	6.3640e-05	-1.2212e-05	4.7947e-05	4.0869e-06	-1.5693e-05
0.6061	-1.6436e-05	6.4268e-05	-1.2305e-05	4.8421e-05	4.1315e-06	-1.5846e-05
0.6162	-1.6577e-05	6.4904e-05	-1.2404e-05	4.8902e-05	4.1721e-06	-1.6001e-05
0.6263	-1.6720e-05	6.5547e-05	-1.2504e-05	4.9389e-05	4.2164e-06	-1.6159e-05
0.6364	-1.6866e-05	6.6199e-05	-1.2607e-05	4.9880e-05	4.2588e-06	-1.6318e-05
0.6465	-1.7015e-05	6.6857e-05	-1.2711e-05	5.0377e-05	4.3033e-06	-1.6480e-05
0.6566	-1.7166e-05	6.7522e-05	-1.2819e-05	5.0879e-05	4.3471e-06	-1.6643e-05
0.6667	-1.7319e-05	6.8194e-05	-1.2927e-05	5.1386e-05	4.3920e-06	-1.6808e-05
0.6768	-1.7475e-05	6.8871e-05	-1.3038e-05	5.1897e-05	4.4367e-06	-1.6974e-05
0.6869	-1.7632e-05	6.9555e-05	-1.3150e-05	5.2413e-05	4.4822e-06	-1.7142e-05
0.6970	-1.7792e-05	7.0244e-05	-1.3264e-05	5.2932e-05	4.5277e-06	-1.7312e-05
0.7071	-1.7953e-05	7.0938e-05	-1.3380e-05	5.3455e-05	4.5737e-06	-1.7483e-05
0.7172	-1.8117e-05	7.1638e-05	-1.3497e-05	5.3983e-05	4.6199e-06	-1.7655e-05
0.7273	-1.8282e-05	7.2342e-05	-1.3615e-05	5.4513e-05	4.6665e-06	-1.7829e-05
0.7374	-1.8448e-05	7.3052e-05	-1.3735e-05	5.5048e-05	4.7133e-06	-1.8004e-05
0.7475	-1.8617e-05	7.3765e-05	-1.3856e-05	5.5585e-05	4.7604e-06	-1.8180e-05
0.7576	-1.8786e-05	7.4483e-05	-1.3979e-05	5.6126e-05	4.8077e-06	-1.8357e-05
0.7677	-1.8957e-05	7.5205e-05	-1.4102e-05	5.6670e-05	4.8553e-06	-1.8536e-05
0.7778	-1.9130e-05	7.5931e-05	-1.4227e-05	5.7216e-05	4.9031e-06	-1.8715e-05
0.7879	-1.9304e-05	7.6661e-05	-1.4352e-05	5.7766e-05	4.9512e-06	-1.8895e-05
0.7980	-1.9479e-05	7.7395e-05	-1.4479e-05	5.8318e-05	4.9995e-06	-1.9076e-05
0.8081	-1.9655e-05	7.8132e-05	-1.4607e-05	5.8873e-05	5.0480e-06	-1.9259e-05
0.8182	-1.9832e-05	7.8872e-05	-1.4735e-05	5.9431e-05	5.0967e-06	-1.9442e-05
0.8283	-2.0010e-05	7.9616e-05	-1.4865e-05	5.9990e-05	5.1456e-06	-1.9626e-05
0.8384	-2.0190e-05	8.0363e-05	-1.4995e-05	6.0553e-05	5.1946e-06	-1.9810e-05
0.8485	-2.0370e-05	8.1113e-05	-1.5127e-05	6.1117e-05	5.2439e-06	-1.9996e-05
0.8586	-2.0552e-05	8.1866e-05	-1.5259e-05	6.1684e-05	5.2934e-06	-2.0182e-05
0.8687	-2.0734e-05	8.2622e-05	-1.5391e-05	6.2253e-05	5.3430e-06	-2.0369e-05
0.8788	-2.0918e-05	8.3381e-05	-1.5525e-05	6.2824e-05	5.3928e-06	-2.0557e-05

Table 3. Tabular summary of the final temporal progression, illustrating spatial error minimization throughout the system's evolution

r	$u_{1,\, i}(r)$	$u_{2,\, i}(r)$	$U_{1,\, i}(r)$	$U_{2,\, i}(r)$	$e_{1,\, i}(r)$	$e_{2,\, i}(r)$
0.8889	-2.1102e-05	8.4142e-05	-1.5659e-05	6.3397e-05	5.4427e-06	-2.0746e-05
0.8990	-2.1287e-05	8.4906e-05	-1.5794e-05	6.3971e-05	5.4928e-06	-2.0935e-05
0.9091	-2.1473e-05	8.5673e-05	-1.5930e-05	6.4548e-05	5.5431e-06	-2.1125e-05
0.9192	-2.1660e-05	8.6442e-05	-1.6066e-05	6.5127e-05	5.5935e-06	-2.1315e-05
0.9293	-2.1847e-05	8.7213e-05	-1.6203e-05	6.5707e-05	5.6441e-06	-2.1506e-05
0.9394	-2.2035e-05	8.7987e-05	-1.6340e-05	6.6289e-05	5.6948e-06	-2.1698e-05
0.9495	-2.2224e-05	8.8763e-05	-1.6478e-05	6.6873e-05	5.7456e-06	-2.1890e-05
0.9596	-2.2414e-05	8.9541e-05	-1.6617e-05	6.7458e-05	5.7966e-06	-2.2083e-05
0.9697	-2.2604e-05	9.0322e-05	-1.6756e-05	6.8045e-05	5.8477e-06	-2.2276e-05
0.9798	-2.2795e-05	9.1104e-05	-1.6896e-05	6.8634e-05	5.8989e-06	-2.2470e-05
0.9899	-2.2986e-05	9.1888e-05	-1.7036e-05	6.9224e-05	5.9502e-06	-2.2665e-05
1	-2.3178e-05	9.2675e-05	-1.7177e-05	6.9815e-05	6.0017e-06	-2.2860e-05

To quantitatively confirm the theoretical findings, the time evolution of the Lyapunov function $V(r)$ is plotted next. The smooth decay behavior serves as a key indicator of synchronization stability under Mittag-Leffler criteria.

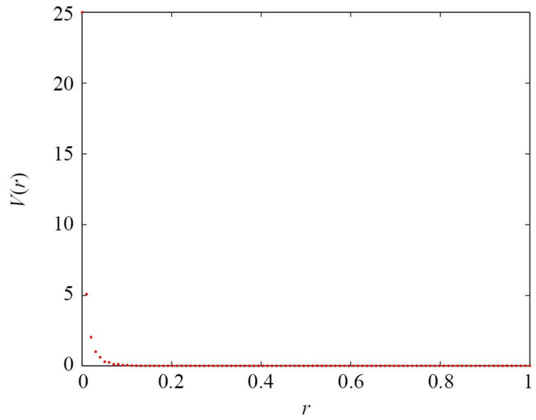

Figure 4. Time evolution of the Lyapunov function $V(r)$ for the linear control scheme. The smooth and monotonic decay toward zero validates Mittag-Leffler stability and confirms convergence of the synchronization error system over time

Finally, to present the error surfaces and control behavior across multiple spatial regions and time intervals, a collection of detailed tables is provided. These tables underscore the convergence trend and the spatial uniformity of the synchronization process.

Table 4. Tabular representation of synchronization error components $e_{1,\,i}(r)$ and $e_{2,\,i}(r)$ across various time steps, illustrating progressive error reduction

r	$V(r)$	r	$V(r)$	r	$V(r)$
0	25	0.2020	7.2826e-05	0.4040	1.1390e-08
0.0101	5.0950	0.2121	2.5450e-05	0.4141	1.0728e-08
0.0202	2.0135	0.2222	1.9196e-05	0.4242	1.0205e-08
0.0303	0.9957	0.2323	6.6419e-06	0.4343	1.0263e-08
0.0404	0.6024	0.2424	5.1480e-06	0.4444	1.0575e-08
0.0505	0.2903	0.2525	1.7600e-06	0.4545	1.0410e-08
0.0606	0.2359	0.2626	1.4264e-06	0.4646	1.0654e-08
0.0707	0.1103	0.2727	4.8228e-07	0.4747	1.0859e-08
0.0808	0.1092	0.2828	4.1986e-07	0.4848	1.0676e-08
0.0909	0.0470	0.2929	1.4257e-07	0.4949	1.0974e-08
0.1010	0.0434	0.3030	1.3760e-07	0.5051	1.1135e-08
0.1111	0.0171	0.3131	4.9802e-08	0.5152	1.1398e-08
0.1212	0.0140	0.3232	5.3950e-08	0.5253	1.1555e-08
0.1313	0.0052	0.3333	2.2833e-08	0.5354	1.1744e-08
0.1414	0.0040	0.3434	2.6723e-08	0.5455	1.1896e-08
0.1515	0.0014	0.3535	1.4498e-08	0.5556	1.2136e-08
0.1616	0.0011	0.3636	1.6918e-08	0.5657	1.2411e-08
0.1717	3.7811e-04	0.3737	1.6948e-08	0.5758	1.2659e-08
0.1818	2.7849e-04	0.3838	1.3019e-08	0.5859	1.2900e-08
0.1919	9.8147e-05	0.3939	1.0616e-08	0.5960	1.3149e-08

Table 5. Supplementary tables illustrating the spatial uniformity of error decay achieved by the linear control strategy

r	$V(t)$	r	$V(t)$
0.6061	1.3439e-08	0.8081	1.9819e-08
0.6162	1.3674e-08	0.8182	2.0198e-08
0.6263	1.3944e-08	0.8283	2.0582e-08
0.6364	1.4221e-08	0.8384	2.0972e-08
0.6465	1.4505e-08	0.8485	2.1367e-08
0.6566	1.4794e-08	0.8586	2.1767e-08
0.6667	1.5090e-08	0.8687	2.2173e-08
0.6768	1.5391e-08	0.8788	2.2584e-08
0.6869	1.5698e-08	0.8889	2.3000e-08
0.6970	1.6010e-08	0.8990	2.3422e-08
0.7071	1.6326e-08	0.9091	2.3849e-08
0.7172	1.6639e-08	0.9192	2.4281e-08
0.7273	1.6938e-08	0.9293	2.4719e-08
0.7374	1.7318e-08	0.9394	2.5162e-08
0.7475	1.7659e-08	0.9495	2.5610e-08
0.7576	1.8005e-08	0.9596	2.6063e-08
0.7677	1.8357e-08	0.9697	2.6522e-08
0.7778	1.8714e-08	0.9798	2.6985e-08
0.7879	1.9077e-08	0.9899	2.7455e-08
0.7980	1.9445e-08	1	2.7929e-08

While the presented results are obtained through controlled simulations of the FHN model, they are strongly motivated by real-world neural dynamics. The adopted spatiotemporal configurations mimic key features observed in biological systems, such as signal propagation delays, localized oscillations, and memory-dependent diffusion behavior in neurons. In particular, the VFO operators used in our model emulate time-varying conductivity and adaptive memory effects commonly seen in cortical tissues and axonal fibers. This is especially relevant in modeling neurodegenerative conditions where signal transmission becomes anomalous due to structural degradation. For instance, the spatial dispersion and decay illustrated in Figures 1-3 resemble wavefront patterns recorded in electrophysiological experiments involving dendritic diffusion or epileptic wave suppression. Moreover, the ability of the control strategy to synchronize two spatiotemporally evolving systems can be mapped onto neural stimulation techniques, such as Deep Brain Stimulation (DBS) or Transcranial Magnetic Stimulation (TMS), where external feedback is used to entrain targeted brain regions. The control terms $C_1(r)$ and $C_2(r)$, in this context, can be interpreted as stimulation inputs designed to restore or maintain coherent neural activity. To simulate experimental uncertainty and physiological variability, the simulations incorporate time-dependent order functions $\theta(r)$, which can be related to bioelectric inhomogeneity or fractal-based neural morphologies observed in Magnetoencephalography (MEG) and functional Magnetic Resonance Imaging (MRI) (fMRI) studies. These realistic, data-driven structures are not explicitly sourced from experimental datasets but reflect empirical trends reported in neuroscientific literature. The current framework could be calibrated using actual neuroimaging datasets or voltage traces recorded from patch-clamp studies to directly assess performance against empirical data. Furthermore, applications in cardiac electrophysiology, where the FHN model also applies, open additional avenues for translating this synchronization framework to control of arrhythmias or signal dispersion in excitable tissues.

5.1.2 *Nonlinear control approach*

For enhanced performance, we consider a nonlinear controller with parameters:

$$\Omega = [0,\ 25], \quad r \in [0,\ 1], \quad (\zeta_1,\ \zeta_2,\ \varpi,\ \varepsilon,\ \gamma,\ N) = \left(0.5,\ 0.3,\ 1,\ 0.3,\ 2.2,\ 1 - 5\times 10^{-6}\sin(0.25),\ 100\right). \tag{53}$$

and initial conditions:

$$\begin{cases} g_1(y_i) = 1.5\left(1+\sin(5\pi y)\right), \quad g_2(y_i) = 2.5\left(1+\cos(5\pi y)\right), \\ \overline{g_1}(y_i) = 1.5\left(1+0.75\sin(\pi y)\right), \quad \overline{g_2}(y_i) = 2.5\left(1+0.9\cos(\pi y)\right). \end{cases} \tag{54}$$

Figures 5 and 6 illustrate the state trajectories of the master and slave systems, while Figure 7 shows the rapid convergence of the synchronization errors. With $\varsigma = 0.6$, the nonlinear control law is:

$$\begin{cases} C_1(r) = -3.36\, e_{1,\ i}(P_r) + e_{2,\ i}(P_r) + 0.6 \left\| \left|U_{1,\ i}(P_r)\right| - \left|u_{1,\ i}(P_r)\right| \right\|, \\ C_2(r) = -0.3\, e_{1,\ i}(P_r) + 0.165\, e_{2,\ i}(P_r), \\ P_r = r + 0.98\left|\sin(\pi t)\right| - 1. \end{cases} \tag{55}$$

Following Theorem 3, Figure 8 confirms Mittag-Leffler synchronization through the evolution of the Lyapunov function. In this subsection as well, all tables (Table 6-10) are explicitly cited in the body of the article to ensure clarity and proper integration with the discussion.

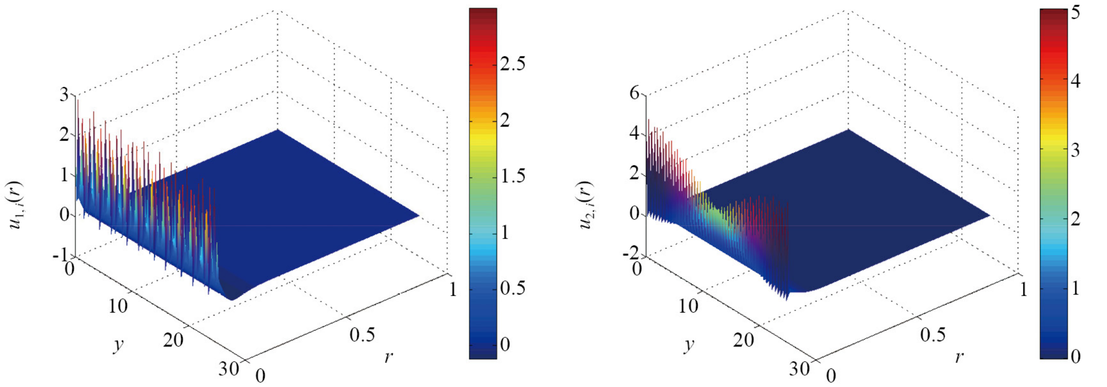

Figure 5. Spatiotemporal trajectories of the master system variables $u_{1,\,i}(r)$ and $u_{2,\,i}(r)$ under nonlinear control. The presence of sharp oscillations reflects the system's response to stronger nonlinear effects in both time r and space y. These behaviors illustrate the increased complexity compared to the linear case

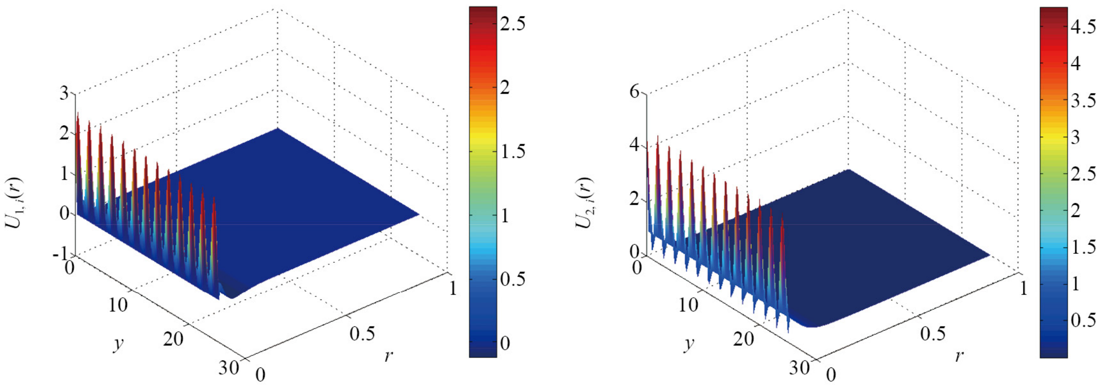

Figure 6. Spatiotemporal trajectories of the slave system variables $U_{1,\,i}(r)$ and $U_{2,\,i}(r)$ under nonlinear control. The trajectories closely replicate the master system dynamics shown in Figure 5, confirming successful synchronization despite strong nonlinear oscillatory behavior across time r and space y

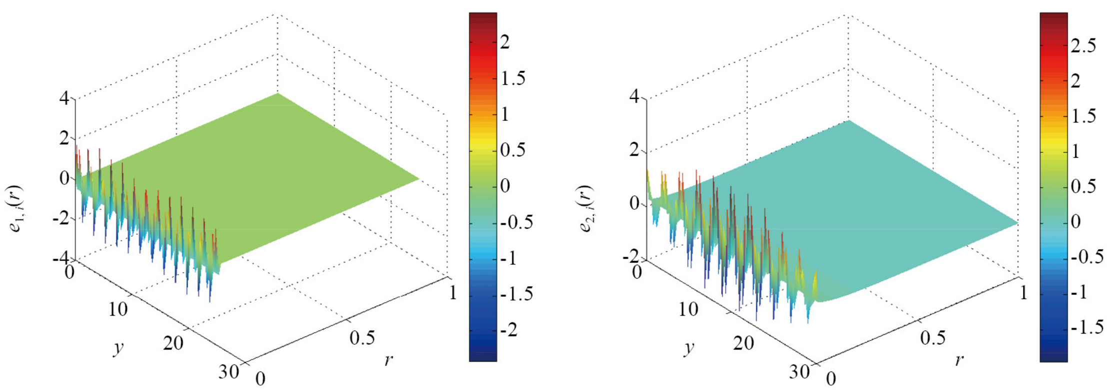

Figure 7. Spatiotemporal trajectories of the synchronization errors $e_{1,\,i}(r) = U_{1,\,i}(r) - u_{1,\,i}(r)$ and $e_{2,\,i}(r) = U_{2,\,i}(r) - u_{2,\,i}(r)$ under nonlinear control. Despite strong initial oscillations, the errors decay rapidly across both time r and space y, confirming effective synchronization

Table 6. Detailed spatiotemporal data of master and slave variables for different time slices under nonlinear control. The rapid convergence across time and spatial layers demonstrates enhanced reactivity to complex dynamics

r	$u_{1,i}(r)$	$u_{2,i}(r)$	$U_{1,i}(r)$	$U_{2,i}(r)$	$e_{1,i}(r)$	$e_{2,i}(r)$
0	0.8986	2.4603	2.5376	3.3693	1.6390	1.6390
0.0101	0.5097	0.4306	-0.0064	0.8751	-0.5161	0.4445
0.0202	0.3714	0.3978	0.3966	0.7873	0.0252	0.3895
0.0303	0.2353	0.3600	0.2437	0.7013	0.0084	0.3413
0.0404	0.1109	0.3183	0.1130	0.6173	0.0022	0.2991
0.0505	0.0094	0.2741	0.0098	0.5361	3.4989e-04	0.2621
0.0606	-0.0614	0.2295	-0.0614	0.4592	2.4347e-05	0.2296
0.0707	-0.1015	0.1871	-0.1015	0.3883	-7.8154e-08	0.2012
0.0808	-0.1175	0.1486	-0.1175	0.3249	5.2019e-08	0.1763
0.0909	-0.1179	0.1153	-0.1179	0.2698	2.1124e-08	0.1545
0.1010	-0.1099	0.0874	-0.1099	0.2228	2.3150e-08	0.1354
0.1111	-0.0979	0.0647	-0.0979	0.1834	2.3181e-08	0.1186
0.1212	-0.0846	0.0467	-0.0846	0.1506	2.3459e-08	0.1039
0.1313	-0.0714	0.0327	-0.0714	0.1237	2.3767e-08	0.0911
0.1414	-0.0591	0.0219	-0.0591	0.1017	2.4078e-08	0.0798
0.1515	-0.0480	0.0139	-0.0480	0.0838	2.4372e-08	0.0699
0.1616	-0.0383	0.0080	-0.0383	0.0693	2.4640e-08	0.0613
0.1717	-0.0300	0.0038	-0.0300	0.0575	2.4876e-08	0.0537
0.1818	-0.0230	9.2111e-04	-0.0230	0.0480	2.5079e-08	0.0471
0.1919	-0.0172	-9.5280e-04	-0.0172	0.0403	2.5250e-08	0.0412
0.2020	-0.0125	-0.0021	-0.0125	0.0340	2.5391e-08	0.0361
0.2121	-0.0088	-0.0027	-0.0088	0.0290	2.5504e-08	0.0317
0.2222	-0.0059	-0.0029	-0.0059	0.0248	2.5593e-08	0.0277
0.2323	-0.0037	-0.0029	-0.0037	0.0214	2.5660e-08	0.0243
0.2424	-0.0020	-0.0027	-0.0020	0.0186	2.5709e-08	0.0213
0.2525	-8.5315e-04	-0.0024	-8.5313e-04	0.0163	2.5744e-08	0.0187
0.2626	-4.6100e-05	-0.0020	-4.6074e-05	0.0143	2.5766e-08	0.0164
0.2727	4.7691e-04	-0.0017	4.7694e-04	0.0126	2.5779e-08	0.0143
0.2828	7.8576e-04	-0.0014	7.8578e-04	0.0112	2.5784e-08	0.0126
0.2929	9.3803e-04	-0.0011	9.3805e-04	0.0099	2.5784e-08	0.0110
0.3030	9.8014e-04	-8.5208e-04	9.8017e-04	0.0088	2.5779e-08	0.0096
0.3131	9.4861e-04	-6.3798e-04	9.4864e-04	0.0078	2.5772e-08	0.0084
0.3232	8.7141e-04	-4.6156e-04	8.7143e-04	0.0069	2.5764e-08	0.0074
0.3333	7.6933e-04	-3.2005e-04	7.6936e-04	0.0062	2.5754e-08	0.0065
0.3434	6.5731e-04	-2.0954e-04	6.5734e-04	0.0055	2.5744e-08	0.0057
0.3535	5.4559e-04	-1.2567e-04	5.4561e-04	0.0049	2.5734e-08	0.0050
0.3636	4.4076e-04	-6.4011e-05	4.4079e-04	0.0043	2.5724e-08	0.0044
0.3737	3.4668e-04	-2.0390e-05	3.4670e-04	0.0038	2.5715e-08	0.0038
0.3838	2.6517e-04	8.9758e-06	2.6519e-04	0.0034	2.5706e-08	0.0034
0.3939	1.9667e-04	2.7384e-05	1.9670e-04	0.0030	2.5697e-08	0.0029
0.4040	1.4068e-04	3.7617e-05	1.4071e-04	0.0026	2.5689e-08	0.0026
0.4141	9.6123e-05	4.1962e-05	9.6149e-05	0.0023	2.5682e-08	0.0023
0.4242	6.1611e-05	4.2249e-05	6.1637e-05	0.0020	2.5674e-08	0.0020
0.4343	3.5653e-05	3.9900e-05	3.5679e-05	0.0018	2.5668e-08	0.0017

To provide a comprehensive evaluation of the nonlinear control strategy, we extend our analysis with high-resolution visualizations that capture the spatiotemporal behavior of the system under stronger nonlinear feedback conditions.

These detailed images offer an in-depth view of the dynamic synchronization process, highlighting the performance enhancements achieved by nonlinear control.

Table 7. Further spatial refinement presenting synchronized trajectory data from additional perspectives, confirming coherence across the domain. The alignment of tabular patterns indicates successful real-time compensation of nonlinear effects

r	$u_{1,\,i}(r)$	$u_{2,\,i}(r)$	$U_{1,\,i}(r)$	$U_{2,\,i}(r)$	$e_{1,\,i}(r)$	$e_{2,\,i}(r)$
0.4444	1.6770e-05	3.5991e-05	1.6796e-05	0.0016	2.5661e-08	0.0015
0.4545	3.5851e-06	3.1311e-05	3.6108e-06	0.0014	2.5655e-08	0.0013
0.4646	-5.1340e-06	2.6415e-05	-5.1084e-06	0.0012	2.5649e-08	0.0012
0.4747	-1.0449e-05	2.1672e-05	-1.0424e-05	0.0010	2.5644e-08	0.0010
0.4848	-1.3250e-05	1.7313e-05	-1.3224e-05	9.1156e-04	2.5638e-08	8.9425e-04
0.4949	-1.4261e-05	1.3464e-05	-1.4235e-05	7.9706e-04	2.5633e-08	7.8360e-04
0.5051	-1.4056e-05	1.0174e-05	-1.4031e-05	6.9682e-04	2.5628e-08	6.8664e-04
0.5152	-1.3081e-05	7.4416e-06	-1,3055e-05	6.0913e-04	2.5623e-08	6.0168e-04
0.5253	-1.1666e-05	5.2335e-06	-1.1640e-05	5.3247e-04	2.5617e-08	5.2724e-04
0.5354	-1.0053e-05	3.4958e-06	-1.0027e-05	4.6550e-04	2.5612e-08	4.6201e-04
0.5455	-8.4084e-06	2.1658e-06	-8.3828e-06	4.0701e-04	2.5607e-08	4.0485e-04
0.5556	-6.8427e-06	1.1786e-06	-6.8171e-06	3.5594e-04	2.5602e-08	3.5476e-04
0.5657	-5.4217e-06	4.7168e-07	-5.3961e-06	3.1134e-04	2.5597e-08	3.1087e-04
0.5758	-4.1792e-06	-1.2038e-08	-4.1536e-06	2.7240e-04	2.5592e-08	2.7241e-04
0.5859	-3.1263e-06	-3.2277e-07	-3.1008e-06	2.3839e-04	2.5587e-08	2.3871e-04
0.5960	-2.2591e-06	-5.0329e-07	-2.2335e-06	2.0868e-04	2.5582e-08	2.0919e-04
0.6061	-1.5635e-06	-5.8899e-07	-1.5379e-06	1.8272e-04	2.5577e-08	1.8331e-04
0.6162	-1.0203e-06	-6.0839e-07	-9.9476e-07	1.6003e-04	2.5572e-08	1.6064e-04
0.6263	-6.0814e-07	-5.8387e-07	-5.8258e-07	1.4019e-04	2.5567e-08	1.4077e-04
0.6364	-3.0513e-07	-5.3249e-07	-2.7957e-07	1.2283e-04	2.5562e-08	1.2337e-04
0.6465	-9.0713e-08	-4.6687e-07	-6.5155e-08	1.0765e-04	2.5557e-08	1.0811e-04
0.6566	5.3697e-08	-3.9601e-07	7.9250e-08	9.4350e-05	2.5552e-08	9.4746e-05
0.6667	1.4429e-07	-3.2603e-07	1.6984e-07	8.2708e-05	2.5547e-08	8.3034e-05
0.6768	1.9474e-07	-2.6080e-07	2.2028e-07	7.2510e-05	2.5542e-08	7.2771e-05
0.6869	2.1627e-07	-2.0257e-07	2.4181e-07	6.3576e-05	2.5537e-08	6.3778e-05
0.6970	2.1786e-07	-1.5234e-07	2.4339e-07	5.5746e-05	2.5532e-08	5.5898e-05
0.7071	2.0650e-07	-1.1029e-07	2.3202e-07	4.8883e-05	2.5527e-08	4.8993e-05
0.7172	1.8746e-07	-7.6034e-08	2.1298e-07	4.2867e-05	2.5522e-08	4.2943e-05
0.7273	1.6462e-07	-4.8870e-08	1.9014e-07	3.7592e-05	2.5517e-08	3.7641e-05
0.7374	1.4070e-07	-2.7909e-08	1.6621e-07	3.2968e-05	2.5512e-08	3.2996e-05
0.7475	1.1752e-07	-1.2209e-08	1.4303e-07	2.8913e-05	2.5507e-08	2.8925e-05
0.7576	9.6208e-08	-8.4696e-10	1.2171e-07	2.5357e-05	2.5502e-08	2.5358e-05
0.7677	7.7384e-08	7.0346e-09	1.0288e-07	2.2239e-05	2.5497e-08	2.2232e-05
0.7778	6.1296e-08	1.2196e-08	8.6787e-08	1.9506e-05	2.5491e-08	1.9493e-05
0.7879	4.7938e-08	1.5292e-08	7.3425e-08	1.7109e-05	2.5486e-08	1.7093e-05
0.7980	3.7146e-08	1.6869e-08	6.2627e-08	1.5007e-05	2.5481e-08	1.4990e-05
0.8081	2.8658e-08	1.7368e-08	5.4133e-08	1.3165e-05	2.5475e-08	1.3148e-05
0.8182	2.2166e-08	1.7142e-08	4.7636e-08	1.1550e-05	2.5470e-08	1.1533e-05
0.8283	1.7353e-08	1.6460e-08	4.2818e-08	1.0135e-05	2.5465e-08	1.0118e-05
0.8384	1.3914e-08	1.5523e-08	3.9373e-08	8.8939e-06	2.5459e-08	8.8784e-06
0.8485	1.1568e-08	1.4476e-08	3.7022e-08	7.8064e-06	2.5454e-08	7.7920e-06
0.8586	1.0070e-08	1.3420e-08	3.5518e-08	6.8534e-06	2.5449e-08	6.8400e-06
0.8687	9.2094e-09	1.2420e-08	3.4652e-08	6.0182e-06	2.5443e-08	6.0058e-06
0.8788	8.8135e-09	1.1515e-08	3.4251e-08	5.2863e-06	2.5438e-08	5.2748e-06

Table 8. Tabular summary of the final temporal progression, illustrating spatial error minimization throughout the system's evolution. Nonlinear feedback ensures rapid attenuation of residual mismatch

r	$u_{1,\,i}(r)$	$u_{2,\,i}(r)$	$U_{1,\,i}(r)$	$U_{2,\,i}(r)$	$e_{1,\,i}(r)$	$e_{2,\,i}(r)$
0.8889	8.7423e-09	1.0723e-08	3.4174e-08	4.6450e-06	2.5432e-08	4.6343e-06
0.8990	8.8859e-09	1.0052e-08	3.4312e-08	4.0831e-06	2.5426e-08	4.0730e-06
0.9091	9.1608e-09	9.4965e-09	3.4582e-08	3.5907e-06	2.5421e-08	3.5812e-06
0.9192	9.5050e-09	9.0482e-09	3.4920e-08	3.1593e-06	2.5415e-08	3.1502e-06
0.9293	9.8745e-09	8.6946e-09	3.5284e-08	2.7813e-06	2.5409e-08	2.7726e-06
0.9394	1.0239e-08	8.4220e-09	3.5643e-08	2.4501e-06	2.5404e-08	2.4417e-06
0.9495	1.0580e-08	8.2169e-09	3.5978e-08	2.1599e-06	2.5398e-08	2.1517e-06
0.9596	1.0886e-08	8.0665e-09	3.6278e-08	1.9056e-06	2.5392e-08	1.8976e-06
0.9697	1.1152e-08	7.9591e-09	3.6538e-08	1.6828e-06	2.5386e-08	1.6749e-06
0.9798	1.1378e-08	7.8849e-09	3.6758e-08	1.4876e-06	2.5380e-08	1.4797e-06
0.9899	1.1565e-08	7.8355e-09	3.6939e-08	1.3166e-06	2.5374e-08	1.3088e-06
1	1.1716e-08	7.8038e-09	3.7084e-08	1.1667e-06	2.5368e-08	1.1589e-06

To quantitatively support the observed synchronization, we present the evolution of the Lyapunov function $V(r)$ over time. The results confirm rapid convergence and improved synchronization speed compared to the linear controller.

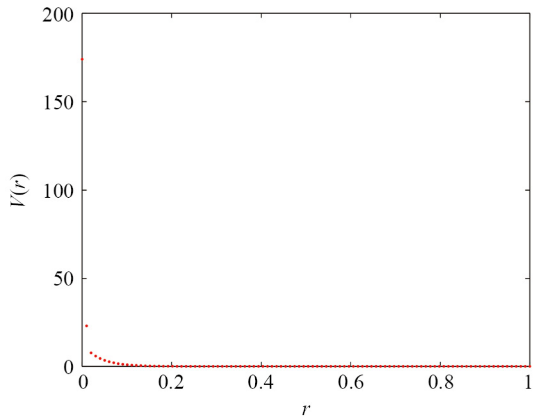

Figure 8. Time evolution of the Lyapunov function $V(r)$ for the nonlinear control scheme. The steep initial drop and rapid convergence to zero demonstrate enhanced Mittag-Leffler stability and superior synchronization performance compared to the linear case

To further highlight the system's convergence properties, we include visualizations of the synchronization error components at multiple time steps. These figures demonstrate consistent spatial uniformity and effective error suppression throughout the simulation domain.

Table 9. Tabular representation of synchronization error components $e_{1,\ i}(r)$ and $e_{2,\ i}(r)$ across various time steps, illustrating progressive error reduction. The temporal layer-wise attenuation validates the control law effectiveness

r	$V(r)$	r	$V(r)$	r	$V(r)$
0	174.0234	0.2020	0.0653	0.4040	3.3096e-04
0.0101	23.1970	0.2121	0.0501	0.4141	2.5412e-04
0.0202	7.6175	0.2222	0.0385	0.4242	1.9512e-04
0.0303	5.8280	0.2323	0.0295	0.4343	1.4982e-04
0.0404	4.4723	0.2424	0.0227	0.4444	1.1503e-04
0.0505	3.4398	0.2525	0.0174	0.4545	8.8525e-05
0.0606	2.6365	0.2626	0.0134	0.4646	6.7819e-05
0.0707	2.0243	0.2727	0.0103	0.4747	5.2074e-05
0.0808	1.5543	0.2828	0.0079	0.4848	3.9898e-05
0.0909	1.1934	0.2929	0.0061	0.4949	3.0701e-05
0.1010	0.9163	0.3030	0.0046	0.5051	2.3574e-05
0.1111	0.7036	0.3131	0.0036	0.5152	1.8101e-05
0.1212	0.5402	0.3232	0.0027	0.5253	1.3899e-05
0.1313	0.4148	0.3333	0.0021	0.5354	1.0672e-05
0.1414	0.3165	0.3434	0.0016	0.5455	8.1590e-06
0.1515	0.2445	0.3535	0.0012	0.5556	6.2827e-06
0.1616	0.1878	0.3636	9.5220e-04	0.5657	4.8320e-06
0.1717	0.1442	0.3737	7.3112e-04	0.5758	3.7104e-06
0.1818	0.1107	0.3838	5.6137e-04	0.5859	2.8492e-06
0.1919	0.0860	0.3939	4.3103e-04	0.5960	2.1880e-06

Table 10. Supplementary illustrations demonstrating the spatial uniformity of error decay achieved by the nonlinear control strategy. The homogeneous error field demonstrates the system's capacity to handle nonlinearities uniformly across space

r	$V(r)$	r	$V(r)$
0.6061	1.6602e-06	0.8081	8.6432e-09
0.6162	1.2900e-06	0.8182	6.5508e-09
0.6263	9.8038e-07	0.8283	6.1169e-09
0.6364	7.6096e-07	0.8384	3.9415e-09
0.6465	5.8414e-07	0.8485	3.0358e-09
0.6566	4.4888e-07	0.8586	2.3396e-09
0.6667	3.4473e-07	0.8687	1.8035e-09
0.6768	2.6478e-07	0.8788	1.3912e-09
0.6869	2.0136e-07	0.8889	1.0738e-09
0.6970	1.5623e-07	0.8990	8.2582e-10
0.7071	1.2000e-07	0.9091	6.4129e-10
0.7172	9.2024e-08	0.9192	4.9628e-10
0.7273	7.0643e-08	0.9293	3.8439e-10
0.7374	5.4435e-08	0.9394	2.9815e-10
0.7475	4.1832e-08	0.9495	2.3612e-10
0.7576	3.2151e-08	0.9596	1.8007e-10
0.7677	2.4714e-08	0.9697	1.4059e-10
0.7778	1.9000e-08	0.9798	1.0228e-10
0.7879	1.4609e-08	0.9899	8.5674e-11
0.7980	1.1236e-08	1	6.7185e-11

Despite its superior synchronization performance, the nonlinear control approach introduces a higher computational burden due to the inclusion of non-smooth terms such as absolute differences and time-varying gains. These terms-while effective at accelerating convergence-require additional resources for real-time evaluation and memory allocation, especially in high-dimensional or long-duration simulations. This computational intensity may pose challenges when deploying the control scheme in embedded systems, neuromorphic chips, or real-time biomedical devices where memory and processing power are limited. Moreover, the evaluation of nonlinear feedback terms at every discrete spatial and temporal step introduces nontrivial overhead, particularly in large-scale networks or fine-grained spatiotemporal meshes. However, this limitation can be effectively mitigated through several strategies:

• **Adaptive Update Frequency:** Rather than applying the nonlinear control law at every iteration, the control can be updated intermittently or based on event-triggered mechanisms, thereby reducing computation while preserving synchronization accuracy.

• **Controller Simplification:** The control terms $C_1(r)$ and $C_2(r)$ can be reformulated using piecewise-linear or smoothed approximations of the absolute-value terms, leading to easier evaluations on digital hardware without significant loss of precision.

• **Parallel Implementation:** Leveraging parallel computing platforms (e.g., GPU or FPGA architectures) can alleviate the computational demand, allowing the nonlinear control law to operate at high speed and low latency-especially in neuroengineering or robotics applications.

• **Domain Reduction:** In practical deployments, full-domain control may be unnecessary. Targeting specific subregions where synchronization is critical can dramatically reduce computational load while maintaining global behavior through diffusion.

• **Offline Precomputation:** In applications with predictable dynamics or repeatable patterns (e.g., prosthetic limb feedback systems or synthetic neuron circuits), control parameters can be pre-tuned offline and stored in compact lookup tables.

From a real-world perspective, the nonlinear controller is particularly well-suited for systems where synchronization speed and robustness outweigh computational constraints. For example, it can be applied in neural prosthetics, epilepsy suppression devices, or brain-machine interfaces, where rapid suppression of error signals is essential. In such cases, the increased control effort is justified by the critical nature of the application. Therefore, while the nonlinear control approach imposes higher computational demands, it also offers superior resilience and faster convergence-qualities that can be harnessed in practical settings using optimized implementations tailored to the application domain.

5.2 *Comparative analysis of linear and nonlinear control performance*

In the linear control scenario, the master system exhibits coherent spatiotemporal patterns that evolve smoothly over the entire spatial domain, as depicted in Figure 1. These trajectories demonstrate the characteristic oscillatory behavior of the FN-RD dynamics under VFO operators. When the same initial conditions are applied to the slave system with the linear feedback law, Figure 2 shows that the slave trajectories closely follow those of the master after an initial transient period. The synchronization errors presented in Figure 3 confirm that discrepancies between the master and slave vanish progressively across both state variables. Notably, the error surfaces decrease uniformly across space, indicating that the linear controller successfully compensates for spatial heterogeneities and nonlinear reaction terms. The monotonic decay of the Lyapunov function in Figure 4 further corroborates this observation: the energy-like measure declines continuously, verifying that synchronization proceeds at a MLS. Overall, the linear control law achieves robust synchronization under the chosen parameter constraints, but the convergence speed is limited by the underlying VFO dynamics and the magnitude of the feedback gains.

In the nonlinear control scenario, the master system again exhibits well-defined spatiotemporal waveforms (Figure 5), while the slave system (Figure 6) responds nearly instantaneously to control interventions. The error surfaces in Figure 7 reveal a markedly faster reduction of discrepancies compared to the linear case. Within only a few time steps, the synchronization layers collapse to zero throughout the spatial domain, illustrating the effectiveness of the nonlinear feedback terms in accelerating convergence. The corresponding Lyapunov estimate in Figure 8 shows a steep initial decline followed by a gradual asymptotic approach to zero, indicating that the nonlinear controller not only enforces rapid error attenuation but also maintains stability as the system approaches perfect synchronization. The augmented term that accounts for the absolute difference between master and slave states proves particularly beneficial in promptly canceling residual mismatches, thereby shortening the settling time relative to the linear counterpart.

Comparative analysis between the two control strategies highlights several important trends. First, while both approaches guarantee eventual synchronization, the nonlinear controller yields a significantly reduced convergence horizon. Second, the nonlinear design demonstrates enhanced robustness to parameter variations, as evidenced by the consistently rapid decay of errors even when the VOF coefficient fluctuates over time. Third, the spatiotemporal coherence of the master dynamics is preserved more faithfully by the nonlinear scheme, which suggests better handling of boundary-induced perturbations and diffusion-driven dispersion. These results emphasize that incorporating nonlinear feedback elements tailored to the intrinsic structure of the error dynamics can substantially improve synchronization performance, especially in systems governed by VOF differences. Despite the clear advantages of the nonlinear controller, several practical considerations remain. The increased computational complexity associated with evaluating absolute-state differences and time-varying VOFs could pose challenges for real-time implementation in high-dimensional domains. In addition, the choice of nonlinear gain parameters requires careful tuning to avoid excessive control effort or undesired oscillations near synchronization. Future work should explore adaptive strategies that adjust these parameters online, as well as investigate the influence of measurement noise and external disturbances on synchronization quality. Nonetheless, the present findings demonstrate that both linear and nonlinear control frameworks are viable for achieving synchronization in discrete VOF-RDs, with the nonlinear approach offering superior speed and resilience under comparable operating conditions.

6. Conclusion

This study has established a rigorous framework for MLSY in coupled VFO-RDs. Through Lyapunov-based analysis, we designed both linear and nonlinear control schemes that guarantee synchronization under explicitly derived parameter constraints. The linear controller provides an analytically tractable solution with proven MLS, while the nonlinear controller achieves accelerated convergence and enhanced robustness to parameter variations. Numerical simulations confirmed that both strategies effectively synchronize the complex spatiotemporal dynamics of the FHN master-slave system, with the nonlinear approach demonstrating superior performance in convergence speed and disturbance rejection. Future research will focus on the following directions:

• Developing adaptive control schemes that autonomously tune FOs and gain parameters in real-time to handle time-varying uncertainties;

• Extending the framework to stochastic systems with measurement noise and external disturbances;

• Investigating multi-dimensional network topologies with delayed coupling;

• Implementing hardware validation for biological and chemical synchronization applications;

• Exploring computational optimizations to reduce the complexity of nonlinear controllers for large-scale or real-time applications.

Additionally, we will explore computational optimizations to address the increased complexity of nonlinear controllers in large-scale systems.

Acknowledgement

The last author (AB) is grateful to Grambling State University for the support he received as the Endowed Chair of Mathematics. This support is sincerely appreciated.

Conflict of interest

The authors declare no competing financial interest.

References

[1] Bendib I, Ouannas A, Dalah M. Mittag-Leffler synchronization of fractional-order reaction-diffusion systems. *Asian Journal of Control*. 2025; 27(5): 1-15. Available from: https://doi.org/10.1002/asjc.3702.

[2] Karoun RC, Ouannas A, Horani MA, Ziar T, Batiha IM, Dibi Z. Chaos in the fractional variable order discrete-time neural networks. In: *2023 International Conference on Fractional Differentiation and Its Applications (ICFDA)*. Ajman, United Arab Emirates: IEEE; 2023. Available from: https://doi.org/10.1109/ICFDA58234.2023.10153184.

[3] Batiha I, Anakira N, Bendib I, Ouannas A, Hioual A, Irianto I, et al. Finite-time analysis of epidemic reaction-diffusion models: Stability, synchronization, and numerical insights. *PLoS One*. 2025; 20(5): e0321132. Available from: https://doi.org/10.1371/journal.pone.0321132.

[4] Batiha IM, Bendib I, Ouannas A, Agarwal P, Anakira N, Jebril IH, et al. Finite-time synchronization in a novel discrete fractional SIR model for COVID-19. *Bulletin of the Paraná Mathematical Society*. 2025; 43(1): 1-15. Available from: https://doi.org/10.5269/bspm.75295.

[5] Batiha IM, Al-Khawaldeh HO, Almuzini M, Alshanti WG, Anakira N, Amourah A. A fractional mathematical examination on breast cancer progression for the healthcare system of Jordan. *Communications in Mathematical Biology and Neuroscience*. 2025; 2025: 29. Available from: https://doi.org/10.28919/cmbn/9138.

[6] Farraj G, Maayah B, Khalil R, Beghami W. An algorithm for solving fractional differential equations using conformable optimized decomposition method. *International Journal of Advances in Soft Computing and Its Applications* 2023; 15(1): 187-196. Available from: https://doi.org/10.15849/IJASCA.230320.13.

[7] Batiha IM, Bendib I, Ouannas A, Jebril IH, Alkhazaleh S, Momani S. On new results of stability and synchronization in finite-time for Fitiz-Nagamo model using grownal inequality and Lyapunov function. *Journal of Robotics and Control*. 2024; 5(6): 1897-1909. Available from: https://doi.org/10.18196/jrc.v5i6.23211.

[8] Djeddi N, Batiha I, Harrouche N, Al-Smadi M, Momani S. Advanced solutions for nonlinear fractional equations: A Laplace-Caputo-RKDM approach. *Gulf Journal of Mathematics*. 2025; 19(2): 93-110. Available from: https: //doi.org/10.56947/gjom.v19i2.2575.

[9] Bouaziz K, Djeddi N, Ogilat O, Batiha IM, Anakira N, Sasa T. Stability analysis of a fractional-order Lengyel-Epstein chemical reaction model. *International Journal of Robotics and Control Systems*. 2025; 5(2): 1539-1551. Available from: https://doi.org/10.31763/ijrcs.v5i2.1848.

[10] Saadeh R, Unami K, Qazza A, Batiha IM, Mohawesh O. Linear fractional differential equations for modeling nonlinear hydro environmental phenomena. *Engineering Letters*. 2025; 33(6): 1913-1918.

[11] Anakira NR, Almalki A, Katatbeh D, Hani GB, Jameel AF, Al Kalbani KS, et al. An algorithm for solving linear and non-linear Volterra Integro-differential equations. *International Journal of Advances in Soft Computing & Its Applications*. 2023; 15(3): 77-83. Available from: https://doi.org/10.15849/IJASCA.231130.05.

[12] Batiha IM, Jebril IH, Alshorm S, Anakira N, Alkhazaleh S. On generalized matrix Mittag-Leffler function. *IAENG International Journal of Applied Mathematics*. 2024; 54(3): 576-580.

[13] Berir M. Analysis of the effect of white noise on the Halvorsen system of variable-order fractional derivatives using a novel numerical method. *International Journal of Advances in Soft Computing and Its Applications*. 2024; 16(3): 294-306. Available from: https://doi.org/10.15849/IJASCA.241130.16.

[14] Lee IH, Jo UI. Pattern formations with Turing and Hopf oscillating pattern in a discrete reaction-diffusion system. *Bulletin of the Korean Chemical Society*. 2000; 21(12): 1213-1216.

[15] Azmy YY, Protopopescu V. On the dynamics of a discrete reaction-diffusion system. *Numerical Methods for Partial Differential Equations*. 1991; 7(4): 385-405. Available from: https://doi.org/10.1002/num.1690070408.

[16] Wentz JM, Bortz DM. Boundedness of a class of spatially discrete reaction-diffusion systems. *SIAM Journal on Applied Mathematics*. 2021; 81(5): 1870-1892. Available from: https://doi.org/10.1137/20M131850X.

[17] Owolabi KM, Atangana A. Numerical simulation of noninteger order system in subdiffusive, diffusive, and superdiffusive scenarios. *Journal of Computational and Nonlinear Dynamics*. 2017; 12(3): 031010. Available from: https://doi.org/10.1115/1.4035195.

[18] Armanyos M, Radwan AG. Fractional-order FitzHugh-Nagumo and Izhikevich neuron models. In: *2016 13th International Conference on Electrical Engineering/Electronics, Computer, Telecommunications and Information Technology (ECTI-CON)*. Chiang Mai, Thailand: IEEE; 2016. Available from: https://doi.org/10.1109/ECTICon.2016.7561406.

[19] Brandibur O, Kaslik E, Mozyrska D, Wyrwas M. Stability results for two-dimensional systems of fractional-order difference equations. *Mathematics*. 2020; 8(10): 1751. Available from: https://doi.org/10.3390/math8101751.

[20] Gafiychuk V, Datsko B. Different types of instabilities and complex dynamics in reaction-diffusion systems with fractional derivatives. *Journal of Computational and Nonlinear Dynamics*. 2012; 7(3): 031001. Available from: https://doi.org/10.1115/1.4005923.

[21] Bendoukha S, Ouannas A, Wang X, Khennaoui AA, Pham VT, Grassi G, et al. The co-existence of different synchronization types in fractional-order discrete-time chaotic systems with non-identical dimensions and orders. *Entropy*. 2018; 20(9): 710. Available from: https://doi.org/10.3390/e20090710.

[22] Armanyos M, Radwan AG, Madian AH. Fractional-order synchronization of two neurons using FitzHugh-Nagumo neuron model. In: *2016 3rd International Conference on Advances in Computational Tools for Engineering Applications (ACTEA)*. Zouk Mosbeh, Lebanon: IEEE; 2016. Available from: https://doi.org/10.1109/ACTEA.2016.7560133.

[23] Ouannas A, Bendoukha S, Khennaoui AA, Grassi G, Wang X, Pham VT. Chaos synchronization of fractional-order discrete-time systems with different dimensions using two scaling matrices. *Open Physics*. 2019; 17(1): 942-949. Available from: https://doi.org/10.1515/phys-2019-0099.

[24] Yang S, Jiang H, Hu C, Yu J. Synchronization for fractional-order reaction-diffusion competitive neural networks with leakage and discrete delays. *Neurocomputing*. 2021; 436: 47-57. Available from: https://doi.org/10.1016/j.neucom.2021.01.009.

[25] Cao Y, Dharani S, Sivakumar M, Cader A, Nowicki R. Mittag-Leffler synchronization of generalized fractional-order reaction-diffusion networks via impulsive control. *Journal of Artificial Intelligence and Soft Computing Research*. 2025; 15(1): 25-36. Available from: https://doi.org/10.2478/jaiscr-2025-0002.

[26] Stamova I, Stamov G. Mittag-Leffler synchronization of fractional neural networks with time-varying delays and reaction-diffusion terms using impulsive and linear controllers. *Neural Networks*. 2017; 96: 22-32. Available from: https://doi.org/10.1016/j.neunet.2017.08.009.

[27] Narayanan G, Ali MS, Karthikeyan R, Rajchakit G, Sanober S, Kumar P. Adaptive strategies and its application in the Mittag-Leffler synchronization of delayed fractional-order complex-valued reaction-diffusion neural networks. *IEEE Transactions on Emerging Topics in Computational Intelligence*. 2024; 8(5): 3294-3307. Available from: https://doi.org/10.1109/TETCI.2024.3375450.

[28] Hussain AS, Pati KD, Atiyah AK, Tashtoush MA. Rate of occurrence estimation in geometric processes with maxwell distribution: A comparative study between artificial intelligence and classical methods. *International Journal on Advanced Soft Computing and Its Applications*. 2025; 17(1): 1-15. Available from: https://doi.org/10.15849/IJASCA.250330.01.

[29] Berir M. Analysis of the Effect of white noise on the halvorsen system of variable-order fractional derivatives using a novel numerical method. *International Journal on Advanced Soft Computing and Its Applications*. 2024; 16(3): 294-306. Available from: https://doi.org/10.15849/IJASCA.241130.16.

[30] Anber AN, Dahmani Z. The laplace decomposition method for solving nonlinear conformable fractional evolution equations. *International Journal of Open Problems in Computer Science and Mathematics*. 2024; 17(1): 67-81.

[31] Anber A, Dahmani Z. The LDM and the CVIM methods for solving time and space fractional Wu-Zhang differential system. *International Journal of Open Problems in Computer Science and Mathematics*. 2024; 17(3): 1-18.

[32] Singh P, Zade N, Priyadarshi P, Gupte A. The application of machine learning and deep learning techniques for global energy utilization projection for ecologically responsible energy management. *International Journal of Advanced Soft Computing and Its Applications*. 2025; 17(1): 49-66. Available from: https://doi.org/10.15849/IJASCA.250330.04.

[33] Mohammed EA, Lakizadeh A. Benchmarking vision transformers for satellite image classification based on data augmentation techniques. *International Journal of Advanced Soft Computing and Its Applications*. 2025; 17(1): 98-114. Available from: https://doi.org/10.15849/IJASCA.250330.06.

[34] Al-Saidi NMG, Natiq H, Baleanu D, Ibrahim RW. The dynamic and discrete systems of variable fractional order in the sense of the Lozi structure map. *AIMS Mathematics*. 2023; 8(1): 733-751. Available from: https://doi.org/10.3934/math.2023035.

[35] Abdeljawad T. On Riemann and Caputo fractional differences. *Computers & Mathematics with Applications*. 2011; 62(3): 1602-1611. Available from: https://doi.org/10.1016/j.camwa.2011.03.036.

[36] Baleanu D, Wu G, Bai Y, Chen F. Stability analysis of Caputo-like discrete fractional systems. *Communications in Nonlinear Science and Numerical Simulation*. 2017; 48: 520-530. Available from: https://doi.org/10.1016/j.cnsns.2017.01.002.

[37] Wei Y, Wei Y, Chen Y, Wang Y. Mittag-Leffler stability of nabla discrete fractional-order dynamic systems. *Nonlinear Dynamics*. 2020; 101: 407-417. Available from: https://doi.org/10.1007/s11071-020-05776-3.

[38] He JH. Two-scale fractal derivative for physical and biological phenomena. *Thermal Science*. 2020; 24(5): 2763-2767.

[39] He JH. A new fractional derivative and its application to nonlinear wave equations. *Thermal Science*. 2012; 16(2): 331-334.

[40] Atangana A, Baleanu D. New fractional derivatives with nonlocal and non-singular kernel: Theory and application to heat transfer model. *Thermal Science*. 2016; 20(2): 763-769.

[41] Wang KL, He CH. A remark on Wang's fractal variational principle. *Fractals*. 2019; 27(8): 1950134. Available from: https://doi.org/10.1142/S0218348X19501342.

[42] He CH, Liu C. Fractal dimensions of a porous concrete and its effect on the concrete's strength. *Facta Universitatis, Series: Mechanical Engineering*. 2023; 21(1): 137-150. Available from: https://doi.org/10.22190/FUME221215005H.

[43] Al-Taani H, Hammad MMA, Alomari O, Bendib I, Ouannas A. Finite-time control of the discrete Sel'kov-Schnakenberg model: Synchronization and simulations. *AIP Advances*. 2025; 15(2): 025325. Available from: https://doi.org/10.1063/5.0257304.

[44] He CH, Liu HW, Liu C. A fractal-based approach to modeling the mechanical properties of recycled aggregate concretes considering the influence of the interfacial transition zone. *Fractals*. 2023; 31(2): 2340024.

[45] Alnabulsi S, Mahmoud W, Bendib I, Ahmad A, Ouannas A, Al-Husban A. Finite-time stability in the discrete Sel'kov-Schnakenberg reaction-diffusion model: Analytical analysis and numerical simulations. *International Journal of Neutrosophic Science*. 2025; 26(4): 155-166. Available from: https://doi.org/10.54216/IJNS.